Angewandte Chemie
Eine Zeitschrift der Gesellschaft Deutscher Chemiker

Supporting Information

Uncovering the Role of Bicarbonate in Calcium Carbonate Formation at Near-Neutral pH

*Yu-Chieh Huang, Ashit Rao, Shing-Jong Huang, Chun-Yu Chang, Markus Drechsler, Jennifer Knaus, Jerry Chun Chung Chan, Paolo Raiteri, Julian D. Gale, and Denis Gebauer**

anie_202104002_sm_miscellaneous_information.pdf

Table of Contents

Experimental Procedures

1 Titration Setup

Potentiometric titration experiments were performed utilizing a computer-controlled system manufactured by Metrohm using the software Tiamo 2.3. The setup is composed of two titration devices (Titrando 809) controlling three dosing devices (800 Dosino) for the automatic dosing of $CaCl_2$, NaOH, and HCl, respectively. A calcium ion-selective electrode (Metrohm No. 6.0508.110) and a pH electrode (Metrohm No. 6.0256.100) were utilized to monitor the calcium potential and pH, respectively. The pH electrode was used as the reference electrode for calcium potential measurements and was calibrated using pH 4.01, pH 7.00, and pH 9.21 Mettler Toledo standard buffers (No. 51302069, No. 51302047, No. 51302070).

2 Experimental Protocol

All solutions were prepared using Milli-Q water. Different concentrations of $CaCl_2$ solutions (10 mM, 20 mM, and 50 mM) and HCl (10 mM and 50 mM) solutions were diluted by using stock solutions of $CaCl_2$ (1.0 M, Fluka, volumetric solution) and HCl (0.1 N, Merck, Titripur® volumetric solution), respectively. The NaOH solution used in constant-pH titrations is a standardized liquid (0.01 N, Alfa Aesar). The carbonate buffers with pH values higher than 8.4 were freshly prepared by mixing appropriate quantities of 10 mM each of $NaHCO_3$ (Carl Roth, ACS grade, ≥ 99.5%) and Na_2CO_3 (Sigma-Aldrich, ACS grade, ≥ 99.8%) solutions in a volume ratio that produces the particular pH value (pH 9.0, 8.8, and 8.5). The carbonate buffers with lower pH levels were freshly prepared using $NaHCO_3$ and the pH values (pH 8.2, 8.0, 7.8, and 7.5) of the buffers were adjusted by adding small aliquots of either 50 mM or 100 mM HCl. Aqueous NaCl solutions (30 mM and 60 mM) were prepared by dissolution of the solid salt (VWR, ACS grade).

In a titration experiment, the $CaCl_2$ solution (10 mM or 20 mM) was continually dosed into carbonate buffer (10 mM or 20 mM, 20 mL) at a constant rate of 20 µl/min under ambient conditions (25ºC) and the pH was kept constant by automatic addition of NaOH and HCl solutions. During the experiment, the titration vessel (150 mL) was closed in order to inhibit CO_2 out-diffusion. The same method was applied for NaCl titration experiments, but the $CaCl_2$ solution was replaced by NaCl solution (30 mM or 60 mM) with identical ionic strength to the corresponding $CaCl_2$ solution (10 mM or 20 mM). A calibration experiment was conducted for calculating the free Ca^{2+} concentration by dosing $CaCl_2$ into Milli-Q water (20 mL) using similar conditions. After each titration experiment, acetic acid (10%, diluted by using 95.9% acetic acid, Carl Roth) was used to eliminate the traces of precipitation in the titration vessel, on the electrodes and on the burette tips. After two washes with acetic acid, the equipment was cleaned by using Milli-Q water and dust-free tissue paper. For each investigated pH, at least three independent experiments were conducted to ensure reproducibility.

3 Cryogenic Transmission Electron Microscopy (Cryo-TEM)

A normalization factor (N) represents the ratio of the time points for sampling to nucleation time in a specific titration run. Prior to and after the nucleation of solid mineral particles (N: 0.8 and 1.1, Figure 2 and Figure S25), samples were drawn from the titration experiments at pH 8.5 and 8.0, were blotted as thin films on lacey carbon filmed copper grids and were vitrified by plunging into liquid ethane by using a temperature- and humidity-controlled plunge-freezing device (Leica EMGP, Wetzlar, Germany). The specimen was transferred with the help of a cryo-holder (CT3500, Gatan, Munich, Germany) and examined in a Zeiss/LEO EM922 Omega EFTEM operated at 200 kV (Carl Zeiss Microscopy GmbH, Jena, Germany). Imaging was performed with a slow-scan CCD camera (Ultrascan 1000, Gatan, Munich, Germany) operated by using a software suite (Digital Micrograph, Gatan, Munich, Germany).

4 Sample Preparation for IR, EDX, SEM, and ssNMR

4.1 Preparation of ACCs

Following the titration protocol, $CaCl_2$ solutions (10 mM, 20 mM, and 50 mM) were slowly dosed into carbonate buffer (10 mM, 20 mM, and 50 mM, 50 mL) at pH 8.5, 8.0, and 7.5, respectively. The buffer solutions at pH 8.5, 8.0, and 7.5 with total volumes of about 55 mL (including the dosed $CaCl_2$ and HCl solutions during titration) were collected at 10800 s, 10000 s, and 8000 s, respectively (before the nucleation of solid mineral particles) and then slowly poured into 1.2 L (around 20 times of mother solutions) 99.95% absolute ethanol (VWR, No. 20821.296). After stirring for 30 minutes in a beaker sealed with Parafilm, the resulting solutions were kept still for 1 hour. Note that a longer incubation time can produce a larger amount of sediment; however, this is associated with an increased risk that the ACC particles might transform into the crystalline phase. The amorphous sediments are transparent and settled at the bottom of the beaker. Significant proportions of the supernatants were aspirated by using an automatic pipette and remaining volumes (about 150–200 mL) were centrifuged at 9000 rpm (7690 g) for 10 min. The transparent pellets obtained were re-suspended in absolute ethanol (100 mL) and then were centrifuged. Subsequently, the re-suspension and centrifugation were repeated by using isopropanol (50 mL, VWR, No. 20842.312) and subsequently with acetone (50 mL, VWR, No. 20066.296) to ensure the removal of water. The resultant ACCs were stored in acetone, which enables the amorphous mineral to be unaffected by non-structural water and to remain stable for at least 3 weeks. Only prior to subsequent experiments, the ACC samples were vacuum dried at 40°C for 30 min. The yields of synthesized specimens at pH 8.5, 8.0, and 7.5 are approximately 0.3–0.5 mg, 0.8–1.0 mg, and 2.5–3.0 mg, respectively.

4.2 Preparation of ^{13}C enriched ACCs

^{13}C-enriched samples were prepared using $NaH^{13}CO_3$ (Cambridge Isotopes, No. CLM-411-5, 99.9% ^{13}C enriched). $NaH^{13}CO_3$ solutions (10 mM, 20 mM, or 50 mM) were prepared and the pH values of these solutions (pH 8.5, 8.0, and 7.5) were adjusted by adding small aliquots of HCl (10 mM, 50 mM, or 100 mM, respectively). The procedure for ACC preparation is described above. For ssNMR measurements, the samples were vacuum dried at 40ºC for 30 minutes and were stored in a desiccator containing molecular sieves in order to mitigate interactions with atmospheric water content and to inhibit crystallization.

4.3 Preparation of Post-Nucleation Sediments

Titration experiments were conducted by using carbonate buffers (20 mL) at pH 9.0, 8.8, 8.5, 8.2, and 8.0. Following the nucleation event, after 1 hour (in the plateau stage), the post-nucleation precipitates were collected by slowly pouring the mineralizing solution into 99.95% absolute ethanol (0.4 L). The collection procedure is the same as mentioned above.

5 FT-IR/ATR Spectroscopy, EDX, and SEM

Fourier transform infrared (FT-IR) spectra were acquired on a PerkinElmer spectrum 100 instrument equipped with an attenuated total reflection (ATR) accessory and recorded in the range of 650–4000 cm^{-1} with a spectral resolution of 4 cm^{-1}. 64 scans were accumulated for the background correction and sample characterization, and for each sample at least two spectra were measured.

The specimens of ACCs synthesized at distinct pH (pH 7.5, 8.0, and 8.5) were placed on silica wafers and characterized by using a desktop SEM (Hitachi TM-3000 SEM, Hitachi High-Technologies Europe GmbH) coupled with an energy dispersive detector (Xcite, Bruker AXS GmbH). The high-resolution images were acquired using a Zeiss CrossBeam 1540XB SEM.

6 TGA and DSC

The thermogravimetric analyses (TGA) and differential scanning calorimetry (DSC) profiles were acquired simultaneously by utilizing Al_2O_3 crucibles at a heating rate of 10 K/min under a nitrogen atmosphere on a STA449F3 Jupiter® instrument.

7 Solid-State Nuclear Magnetic Resonance

Experiments involving ^{13}C direct excitation and $^{13}C\{^1H\}$ cross-polarization were carried out at ^{13}C and ^1H frequencies of 100.7 and 400.1 MHz, respectively, whereas the $^{13}C\{^1H\}$ heteronuclear correlation (HETCOR) spectra were acquired at ^{13}C and ^1H frequencies of 150.9 and 600.2 MHz, respectively, on Bruker Avance III spectrometers equipped with commercial 3.2 mm probeheads. ^{13}C chemical shifts were externally referenced with adamantane as the secondary reference. The MAS frequency was 12 kHz and the measurements were conducted at 273 K. For ^{13}C direct excitation (Bloch decay) experiments, the recycle delay was set to 350 s. For the $^{13}C\{^1H\}$ cross-polarization experiments, the ^1H nutation frequency was set to 50 kHz and that of ^{13}C was ramped linearly through the Hartmann-Hahn matching condition. Two pulse phase modulation (TPPM)[1] proton decoupling of 75 kHz was applied during the acquisition period. The $^{13}C\{^1H\}$ HETCOR spectra were acquired under the conditions of frequency-switched Lee-Goldburg (FSLG)[2] irradiation during the t_1 evolution to enhance the spectral resolution in the ^1H dimension. The FSLG irradiation was achieved by setting the ^1H decoupling field and the resonance offset at 90 and 63.64 kHz, respectively, so that the effective nutation frequency was equal to 110.2 kHz. The spectrum was acquired at a spin rate of 12 kHz. For each t_1 increment, 1024 transients were accumulated and a total of 32 increments were at steps of 41.96 µs. The contact time for cross-polarization was set to 0.5 ms.

8 Computer Simulation

8.1 Determination of the Equilibrium Constants for Bicarbonate Speciation

The stability of complexes between the bicarbonate anion and calcium ions in aqueous solution have been determined via the use of molecular dynamics simulations. While we have previously created a rigid-ion force field that spanned all of the species required for the present work, this model tended to overstabilize the calcium bicarbonate ion pair[3]. Hence, we have created a new and more accurate force field for the present work based on the polarizable AMOEBA model[4]. Parameters for the carbonate and bicarbonate anions were generated using gas phase quantum mechanical calculations according to the standard protocol in order to determine the molecular geometry, charge distributions, and multipoles. The short-range interaction parameters between calcium, carbonate and bicarbonate and water were then adjusted in order to reproduce the free energies of hydration for each ion, while also comparing the solvation structure to that obtained from *ab initio* molecular dynamics. The AMOEBA force field was supplemented by the addition of a Buckingham potential between calcium and the oxygens of both carbonate and bicarbonate. For the Ca-CO_3 interactions, the Buckingham parameters were adjusted to reproduce the free energy difference between calcite and the aqueous ions, as given by the experimental solubility, leading to parameters *A* = 3687.67 kcal/mol and ρ = 0.3 Å. Full details of the derivation of the model for carbonate can be found elsewhere.[5] In the case of Ca-HCO_3 there is no corresponding mineral phase to calibrate against and so only the *A* parameter was fitted against the gas phase binding geometry and energy computed at the ωB97X-D3/ma-def2-QZVPP level of theory[6–8], yielding a value of *A* = 1729.58 kcal/mol. The full set of AMOEBA parameters used are given in Tinker format.

All molecular dynamics simulations with the AMOEBA force field have been performed with TINKER HP[9] code and a box of approximately 25 Å in size containing the ions and 511 water molecules. All simulation boxes were initially equilibrated in the NPT ensemble at 1 atm and a temperature of 300 K. A cell with the equilibrated average volume was then used for all subsequent simulations. The equations of motion were integrated with the velocity Verlet algorithm and a 1 fs timestep, and the temperature was controlled with the Canonical Sampling through Velocity Rescaling algorithm. The ion solvation free energies were computed with the Free Energy Perturbation and BAR methods as implemented in TINKER while the pairing free energies were computed using the open-source, community-developed PLUMED library,[10] version 2.5.[11] The TINKER-PLUMED interface was developed for this work and has now been included in the official TINKER HP distribution. The real space interactions were truncated at 9 Å, the Ewald summation was used for the long-range electrostatics, and the atom polarizations were converged self-consistently at every timestep with a threshold of 10^{-5}.

All pairing free energies were computed with the Multiple Walkers Well-Tempered Metadynamics algorithm[11–14] using the Ca-C distance as the collective variable. Gaussians were deposited every 1 ps with an initial height of 0.6 kcal/mol, a width of 0.2 Å and a bias factor of 5 was used to ensure convergence of the calculations. The alignment of the free energy and conversion to standard conditions was handled as described previously[15]. For species with multiple ions, restraints were applied to Ca-C distances such that the free energy for association of further ions could be mapped using a single collective variable. The restraint had the form of a harmonic potential between the calcium and carbon atoms. The harmonic potential was centered at a distance of 3 Å for calcium-carbonate interactions and 3.2 Å for the calcium-bicarbonate, with a spring constant of 5 kcal/mol/Å^2, and was applied only for distances larger than the equilibrium distance. Preliminary calculations, however, showed that the pairing free energy was not very sensitive to the choice of the restraining potential, provided that the cluster did not break during the simulation, analogously to our recent work on the study of calcium phosphate clusters using a similar approach.[16] Figure S10 shows the computed Ca-HCO_3^+ binding free energies as a function of temperature aligned to the known analytic solution for the pairing free energy of two point particles interacting via an electrostatic potential screened by a medium with the dielectric constant of the AMOEBA 03 water potential.[17]

The binding free energies obtained from the force field simulations were also used to estimate the change in pK_a of the bicarbonate ion as a function of its' environment. In order to further validate the simulation results, *ab initio* quantum mechanical calculations were also performed to confirm the results for the $CaHCO_3^+$ ion pair and $Ca_2HCO_3^{3+}$. Here we have used calculations at the ωB97X-D3/ma-def2-QZVPP level of theory, as implemented in the ORCA code[18], with numerical integration using Grid4. The RIJ-COSX approximation[19] was used to accelerate the early stages of geometry optimization, though all final results were computed without use of resolution of the identity. All calculations were performed with species embedded in the conductor-like polarizable continuum (CPCM) model[20] with a dielectric constant of water. Default radii were used for all elements except calcium, where the value was fitted to be more appropriate to the hydration free energy of Ca^{2+}, leading to a radius of 1.824 Å. An explicit first shell of water molecules was included for all species to improve the accuracy of the solvation description. The energies used to calculate the pK_a consisted of the electronic internal energy plus the zero point contribution from the vibrational frequencies. Thermal contributions to the vibrational free energy were not included since these are dominated by the low-frequency modes, which are the least accurately described feature in the cluster-continuum description of the ions in the liquid phase.

8.2 Generation of Models for Amorphous Calcium Carbonate

There have been numerous previous experimental and computational studies of the structure of amorphous calcium carbonate (ACC).[21,22] While there is consistent agreement as to the averaged pair distribution function, there have been different proposals for the details of the disordered structure. For example, Goodwin *et al*.[21] proposed that for hydrated ACC, the water formed a network of channels between drier framework regions. This was supported by simulations that showed the thermodynamically favored water content within nanoparticles of ACC varied with particle size.[23] While Goodwin *et al*. provided the coordinates for two structural models of ACC based on Reverse Monte Carlo, neither set is suitable for the present study for two reasons: Firstly, one of the sets of coordinates contains unphysical overlaps between carbonate groups; secondly, the size of the unit cell is prohibitive for current quantum mechanical calculations and therefore the determination of chemical shifts. Similarly, all other previously generated simulation models of ACC that we are aware of were designed for the use of force field-based techniques and therefore employed system sizes that are too large for the present purposes. Hence, in the present study, it was necessary to generate new structural models for ACC that utilize relatively small unit cell dimensions. While it is recognized that this is an approximation that will lead to errors in describing the long-range structure, it should provide reasonable local environments, as primarily probed by ssNMR chemical shifts.

In this study, models for both dry ACC and a more relevant wet ACC with a composition of $CaCO_3.H_2O$ were generated, close to that measured in the present experiments. In both cases, nanoparticles were initially simulated at high temperature in the gas phase using force field methods based on the latest interatomic potentials of Raiteri *et al*.[15] For dry ACC, an initial particle containing 56 formula units of $CaCO_3$ (280 atoms) was chosen. This initial cluster was then placed in a cubic box of side length 50 Å. Molecular dynamics in the NPT ensemble with orthorhombic constraints was then performed at 500 K with a pressure of 1 GPa in order to gradually form a dense amorphous phase using a timestep of 1 fs. Once the system had reached a stable density, it was further annealed at 300 K and without any external pressure in order to locally equilibrate the structure. A similar procedure was used to generate the model for wet ACC, except that the particle of $CaCO_3$ contained 36 formula units, and when initially placed in the cubic box was surrounded by 36 water molecules, resulting in a similar system size to the dry case (288 atoms). This naturally leads to a model for wet ACC that is consistent with the hypothesis of Goodwin *et al*.[21], in which the distribution of water is inhomogeneous. As will be described in the next section, these initial force field generated models only provided a starting point and were ultimately relaxed at the same level of theory used for the calculation of the NMR chemical shifts.

8.3 Quantum Mechanical Calculations of Chemical Shifts

All quantum mechanical calculations have been performed using the plane-wave pseudopotential approach within Kohn-Sham density functional theory as implemented in the program CASTEP[24]. Here the Generalized Gradient Approximation (GGA) of Perdew-Burke-Ernzerhof (PBE) was used in conjunction with the semi-empirical dispersion correction of Grimme[25], as implemented by McNellis *et al*.[26]. Core electrons and nuclei are represented using ultra-soft pseudopotentials that are generated on the fly with a small core for Ca. A plane-wave cut-off of 800 eV was used for all calculations. The Brillouin zone for crystalline phases was sampled using a Monkhorst-Pack mesh with a k-point separation tolerance of 0.04 $Å^{-1}$. In the case of the models for ACC, the unit cell parameters were sufficiently large such that for this insulating material only the gamma point was necessary.

All structures have been optimized using the L-BFGS algorithm with respect to the unit cell and internal coordinates. In the case of the amorphous models, the unit cell was relaxed under orthorhombic constraints. The tolerances for the forces and stresses for crystalline structures were 0.02 eV/Å and 0.25 GPa, respectively, while the total energy was converged to better than 2.5×10^{-5} eV during relaxation. For the amorphous systems, it was necessary to use a higher force tolerance of 0.05 eV/Å to achieve convergence, though all other criteria were met without change.

Calculation of the chemical shielding tensor was performed using the approach of Yates *et al*.[27], based on the gauge-including projector augmented wave approach of Pickard and Mauri[28]. The isotropic shielding values were then converted to ^1H and ^{13}C chemical shifts using a reference system. Here the mineral nahcolite ($NaHCO_3$) was chosen as the reference since the objective is to study the bicarbonate ion as a defect in calcium carbonate phases. Nahcolite contains a single symmetry-unique resonance for both hydrogen and carbon, thereby avoiding any ambiguities relating to peak assignment.

In order to determine the range of possible chemical shifts for bicarbonate in ACC, several defect calculations were performed where a proton was added to different carbonate groups within the structure. In each case, the internal coordinates were fully optimized while keeping the cell dimensions fixed at those of the non-defective material. The excess charge of the proton was compensated through the use of a uniform neutralizing background charge. As an alternative, the introduction of a charge-compensating substitution of Na^+ for Ca^{2+} at a site remote from bicarbonate was also explored, though the difference in chemical shift was always < 0.3 ppm.

Results and Discussion

1 Data Evaluation

1.1 Assessment of Bound CO_3^{2-} Ions based on Constant-pH Titrations

The association of Ca^{2+} ions and carbonate species, CO_2 out-diffusion, and the nucleation process altogether lead to changes in the pH levels, which alter the ratio of carbonate species in the system. For quantitative analyses, it is important to maintain a constant pH indicating a fixed ratio of CO_3^{2-} and HCO_3^- species during the titration experiments. Thus, in the present study, the quantitative evaluation is based on the condition of constant pH. During the pre-nucleation stage, equilibrium [1] represents the (bi)carbonate buffer equilibrium, wherein the fractional numbers $\lambda(HCO_3^-)$ and $\lambda(CO_3^{2-})$ of HCO_3^- and CO_3^{2-} ions, respectively, can be used to calculate the amount of H^+ generated by the buffer equilibrium upon binding. When one CO_3^{2-} ion is removed from the equilibrium, $[2\lambda(\mathrm{CO_{3,aq}^{2-}})_{\mathrm{pH}} + \lambda(\mathrm{HCO_{3,aq}^{-}})_{\mathrm{pH}}]\mathrm{OH^-}$ ions are automatically dosed in order to keep pH constant.[29] From the amount of NaOH addition during the titration experiments, the amount of bound CO_3^{2-} ions ($\mathrm{n_{bound}(CO_3^{2-})_{NaOH}}$) constituting the pre-nucleation clusters and nucleation products can be calculated (Equation [2]);

$$\mathrm{CO_{2,aq} + H_2O \leftrightharpoons H_2CO_{3,aq} \leftrightharpoons H_{aq}^+ + HCO_{3,\,aq}^- \leftrightharpoons 2H_{aq}^+ + CO_{3,aq}^{2-}} \quad [1]$$

$$\mathrm{n_{bound}(CO_3^{2-})_{NaOH} \cong c(NaOH) \cdot V(NaOH) \cdot \frac{1}{2\lambda(CO_{3,aq}^{2-})_{pH} + \lambda(HCO_{3,aq}^{-})_{pH}}} \quad [2]$$

where c(NaOH) and V(NaOH) denote the concentration and the volume of NaOH, respectively. $\lambda(\mathrm{HCO_{3,aq}^-})_{\mathrm{pH}}$ and $\lambda(\mathrm{CO_{3,aq}^{2-}})_{\mathrm{pH}}$ represent the fractional number of HCO_3^- and CO_3^{2-} species, respectively, and the index ‘pH’ indicates that they depend on the pH value of the solution.

In titrations performed below pH 8.5, we found that CO_2 out-diffusion occurs during titration, which shifts the equilibrium towards CO_2 and causes an increase of pH levels. Simultaneously, Ca^{2+} ions bind to CO_3^{2-} ions and protons are released in the system, leading to a decrease of the pH value. In the pre-nucleation regime for experiments conducted below pH 8.5, HCl is automatically titrated to maintain a constant pH, showing that the outgassing effect is dominant over carbonate binding. However, when mineral nucleation occurs, HCl addition stops and NaOH begins to be dosed, indicating that ion binding prevails at this stage (Figure S3). Since the pH developments during titrations are affected by both CO_2 out-diffusion (represented by HCl addition) and ion binding (represented by HCl or NaOH addition for bicarbonate binding (see below) and NaOH addition for carbonate binding), which compete during titration, the amount of NaOH addition does not represent the entire fraction of bound CO_3^{2-} ions. To determine the actual amount of bound CO_3^{2-} ions during titration, experiments were performed in which the $CaCl_2$ solution (10 mM or 20 mM) was replaced by NaCl solutions (30 mM or 60 mM) with identical ionic strength. In the NaCl titrations, we consistently observed higher contents of HCl required to balance the out-diffusion of CO_2 (Figure S4). From the difference between the HCl additions in these two titrations (i.e., in which $CaCl_2$ and NaCl are dosed), one can determine the missing NaOH titration which corresponds to bound CO_3^{2-} ions for mineral formation ($\mathrm{n_{bound}(CO_3^{2-})_{HCl}}$, Equation [3]);

$$\mathrm{n_{bound}(CO_3^{2-})_{HCl}} \cong \frac{\mathrm{c(HCl)\cdot\left[V(HCl_{NaCl})-V(HCl_{CaCl_2})\right]}}{\mathrm{2\lambda(CO_{3,aq}^{2-})_{pH}+\lambda(HCO_{3,aq}^{-})_{pH}}} \quad [3]$$

where c(HCl) is the concentration of HCl. $\mathrm{V(HCl_{NaCl})}$ and $\mathrm{V(HCl_{CaCl_2})}$ represent the volumes of added HCl required to balance CO_2 out-diffusion in NaCl and $CaCl_2$ titration experiments, respectively. Thus, the amount of added HCl and NaOH during the titration experiments was applied for the quantitation of bound CO_3^{2-} ions. In Figure S7, the red lines represent the total amount of bound CO_3^{2-} ions ($\mathrm{n_{bound}(CO_3^{2-})}$, calculated according to Equation [4]):

$$\mathrm{n_{bound}(CO_3^{2-}) = n_{bound}(CO_3^{2-})_{NaOH} + n_{bound}(CO_3^{2-})_{HCl}} \quad [4]$$

1.2 On the pH Effects upon Bicarbonate Binding

The amount of bound calcium and carbonate do not overlay completely (Figure S7), indicating the mechanistic contributions of HCO_3^- ion binding during the reaction of calcium carbonate nucleation. To deduce whether bicarbonate binding affects mineral nucleation, we initially neglect the effects of bicarbonate binding on the pH development and derive the amount of NaOH ($\mathrm{n_0(OH^-)}$) utilized in the system from the rates of NaOH and HCl addition (Equation [5]), which facilitates the evaluation of the total amount of bound CO_3^{2-} (Equation [6]);

$$\mathrm{n_0\,(OH^-) = c(NaOH)\cdot V(NaOH) + c(HCl)\cdot\left[V(HCl_{\,NaCl}) - V(HCl_{\,CaCl_2})\right]} \quad [5]$$

$$\mathrm{n_{bound}(CO_3^{2-})_0} = \frac{\mathrm{n_0(OH^-)}}{\mathrm{2\lambda(CO_{3,aq}^{2-})_{pH} + \lambda(HCO_{3,aq}^{-})_{pH}}} \quad [6]$$

We assume that the binding of calcium and carbonate species is 1:1, as thoroughly demonstrated for pH 9.0 elsewhere[29,30]. Thus, the amount of bound HCO_3^- ions ($\mathrm{n_{bound}(HCO_3^-)}$) can be assessed by the difference between the amount of bound Ca^{2+} ($\mathrm{n_{bound}(Ca^{2+})}$) and bound CO_3^{2-} ions ($\mathrm{n_{bound}(CO_3^{2-})}$) (Equation [7]);

$$\mathrm{n_{bound}(HCO_3^-) = n_{bound}(Ca^{2+}) - n_{bound}(CO_3^{2-})} \quad [7]$$

The number of protons ($\mathrm{n_0(H^+)}$) generated due to bicarbonate binding is accessible by the following formula in an iterative method (Equation [8]). However, the number of protons generated by bicarbonate binding is negligible.

$$\mathrm{n_0(H^+) = n_{bound}(HCO_3^-)_0} \times \frac{\mathrm{\lambda(CO_{3,aq}^{2-})_{pH}}}{\mathrm{\lambda(HCO_{3,aq}^{-})_{pH}}} \quad [8]$$

Iteration:

$$\mathrm{n_1(OH^-) = n_0(OH^-) + n_0(H^+)}$$

$$\mathrm{n_{bound}(CO_3^{2-})_1} = \frac{\mathrm{n_1\,(OH^-)}}{\mathrm{2\lambda(CO_{3,aq}^{2-})_{pH} + \lambda(HCO_{3,aq}^{-})_{pH}}}$$

$$\mathrm{n_{bound}(HCO_3^-)_1 = n_{bound}(Ca^{2+}) - n_{bound}(CO_3^{2-})_1}$$

$$\mathrm{n_1\,(H^+) = n_{bound}(HCO_3^-)_1} \times \frac{\mathrm{\lambda(CO_{3,aq}^{2-})_{pH}}}{\mathrm{\lambda(HCO_{3,aq}^{-})_{pH}}}$$

$$\mathrm{\Delta n_0(H^+) = n_1(H^+) - n_0(H^+)}$$

$$n_2(OH^-) = n_1(OH^-) + \Delta n_0(H^+)$$

$$n_z(OH^-) = n_{z\text{-}1}(OH^-) + \Delta n_{z\text{-}0}(H^+)$$

After a few iterations, the $\Delta n_{z\text{-}0}(H^+)$ values gradually converge to zero.

1.3 Out-Diffusion of CO_2

For titrations in which NaCl instead of $CaCl_2$ solutions were dosed into a carbonate buffer, the added amount of HCl represents the amount of outgassed CO_2 ($n_{outgassing}(CO_2, t)$), Equation [9], Figure S5, light blue line);

$$n_{outgassing}(CO_2, t) = V(HCl_{NaCl}, t) \cdot c(HCl) \quad [9]$$

where $V(HCl_{NaCl}, t)$ represents the volume of added HCl and $c(HCl)$ represents the concentration of HCl.

Due to nucleation events, the concentrations of carbonate species in the buffer solutions significantly decrease. The out-diffusion still occurs during nucleation and after nucleation, though, is less significant due to the lowered buffer concentration upon precipitation caused by ion binding to the solid calcium carbonate phases. From Equation [10], we can evaluate the concentration of the carbonate buffer ($c(\text{carbonate}, t)$) after the nucleation event;

$$c(\text{carbonate}, t) = \frac{[n_{total}(\text{carbonate}, t{=}0) - n_{bound}(Ca^{2+}, t)]}{V(t)} \quad [10]$$

where $n_{total}(\text{carbonate}, t{=}0)$ denotes the initial amount of carbonate species. $n_{bound}(Ca^{2+}, t)$ represents the amount of bound Ca^{2+} ions with time. $V(t)$ is the total volume of solution at a particular point in time.

At the point in time corresponding to the drop in free Ca^{2+} to a plateau, the concentrations of carbonate buffers at pH 8.5, 8.2, and 8.0 are approximately 7, 15, and 13 mM, respectively. NaCl solutions were titrated into corresponding concentrations of carbonate buffers at a given pH, which enables the out-diffusion curve at the post-nucleation stage to be assessed (Figure S5, light green line). The out-diffusion curve during nucleation was interpolated by the curves in the pre-nucleation regime and post-nucleation regime (Figure S5, dashed red line). From the addition of HCl for balancing CO_2 out-diffusion in carbonate buffers at particular pH conditions, the amount of outgassed CO_2 can be calculated. As seen in Figure S6, the CO_2 out-diffusion becomes more and more significant as the pH level decreases.

1.4 Multiple-Binding Equilibrium

A so-called multiple-binding model, first utilized for protein-ligand systems[31], was applied to evaluate the thermodynamics of calcium carbonate ion association into clusters prior to mineral nucleation from a microscopic perspective[3,29]. In the model, a CO_3^{2-} ion acts as a central ion that contains several binding sites for Ca^{2+} ions (binding ions). It is based on the assumption that the independent binding events are equal and have identical equilibrium constants (K_1), illustrated as below[29].

$$CO_3^{2-} \underset{K_1}{\overset{+Ca^{2+}}{\leftrightharpoons}} CaCO_3 \underset{K_1}{\overset{+Ca^{2+}}{\leftrightharpoons}} [Ca_2CO_3]^{2+} \underset{K_1}{\overset{+Ca^{2+}}{\leftrightharpoons}} \ldots [I]$$

According to the scheme [I];

$$\frac{n_{bound}(Ca^{2+})_{carbonate}}{n_{bound}(CO_3^{2-}) + n_{free}(CO_3^{2-})} = x_1 \frac{K_1 \cdot c_{free}(Ca^{2+})}{1 + K_1 \cdot c_{free}(Ca^{2+})} \quad [11]$$

where x_1 signifies the number of binding sites of a CO_3^{2-} ion for Ca^{2+} ions and K_1 represents the microscopic equilibrium constant of calcium carbonate. $n_{bound}(Ca^{2+})_{carbonate}$ is the amount of Ca^{2+} bound to CO_3^{2-} ions. $n_{bound}(CO_3^{2-})$ and $n_{free}(CO_3^{2-})$ are the amounts of bound and free CO_3^{2-} ions, respectively. $c_{free}(Ca^{2+})$ denotes the concentration of free Ca^{2+} ions in the system.

Since $n_{bound}(Ca^{2+})_{carbonate}$ is equivalent to $n_{bound}(CO_3^{2-})$ and with $\nu = \frac{n_{bound}(CO_3^{2-}) + n_{free}(CO_3^{2-})}{n_{bound}(Ca^{2+})_{carbonate}} = 1 + \frac{n_{free}(CO_3^{2-})}{n_{bound}(CO_3^{2-})}$, the equation [11] can be rewritten as;

$$\nu = \frac{1}{x_1} + \frac{1}{x_1 \cdot K_1} \cdot \frac{1}{c_{free}(Ca^{2+})} \quad [12]$$

$\mathrm{n_{bound}(CO_3^{2-}, t)}$, $\mathrm{c_{free}(Ca^{2+}, t)}$ and $\mathrm{n_{free}(CO_3^{2-}, t)}$ are required for estimating the values of x_1 and K_1. $\mathrm{n_{bound}(CO_3^{2-}, t)}$ is accessible from the time development of NaOH and HCl addition (Equation [4]). $\mathrm{c_{free}(Ca^{2+}, t)}$ is evaluated from the calcium potential measurements. During titration, CO_2 diffuses out from the carbonate buffer. Thus, when calculating the temporal development of the amount of free CO_3^{2-} ions ($\mathrm{n_{free}(CO_3^{2-}, t)}$), the amount of out-diffused CO_2 ($\mathrm{n_{outgassing}(CO_2, t)}$) needs to be applied as a correction (Equation [13]);

$$\mathrm{n_{free}(CO_3^{2-}, t) = \lambda(CO_{3,\,aq}^{2-})_{pH}\left[n_{total}(carbonate, t{=}0) - n_{bound}(Ca^{2+}, t) - n_{outgassing}(CO_2, t)\right]} \quad [13]$$

where $\mathrm{n_{total}(carbonate, t{=}0)}$ represents the total amount of carbonate species in the solution at the beginning of titration. $\mathrm{n_{bound}(Ca^{2+}, t)}$ denotes the amount of bound Ca^{2+} ions with time, which is equivalent to the total amount of bound CO_3^{2-} and HCO_3^- species. $\mathrm{\lambda(CO_{3,\,aq}^{2-})_{pH}}$ represents the fractional number of CO_3^{2-} species.

The mean values of $\mathrm{n_{bound}(CO_3^{2-}, t)}$, $\mathrm{n_{free}(CO_3^{2-}, t)}$ and $\mathrm{c_{free}(Ca^{2+}, t)}$ were fitted by means of linear regression for the data in the pre-nucleation regime. From the plots of ν and the reciprocal of free calcium concentration ($\mathrm{c_{free}(Ca^{2+})}$), the binding parameters, x_1 and K_1, are accessible (Table S3). In the macroscopic perspective ($x_1 = 1$), the equilibrium constant of calcium carbonate ion pairs in clusters (K_1') can be obtained from the product of x_1 and K_1.

$$\mathrm{Ca_{aq.}^{2+} + CO_{3,\,aq.}^{2-} \overset{K'_1}{\leftrightharpoons} [CaCO_3^0]_{cluster,\,aq.}}$$

$$\mathrm{K_{CaCO_3^0} = \frac{c([CaCO_3^0]_{cluster,\,aq.}, t)}{c(Ca_{aq.}^{2+},\ t)\cdot c(CO_{3,\,aq.}^{2-}, t)} \cong K_1' = x_1 \cdot K_1} \quad [14]$$

where $\mathrm{c(Ca_{aq.}^{2+})}$ and $\mathrm{c(CO_{3,\,aq.}^{2-})}$ signify the concentration of free Ca^{2+} and CO_3^{2-}, respectively. $\mathrm{c([CaCO_3^0]_{cluster,\,aq.})}$ represents the concentration of bound CO_3^{2-} species.

We further utilized the multiple-binding model to elucidate the calcium bicarbonate ion association. The scheme is demonstrated as below;

$$\mathrm{CO_3^- \underset{K_2}{\overset{+Ca^{2+}}{\leftrightharpoons}} [CaHCO_3]^+ \underset{K_2}{\overset{+Ca^{2+}}{\leftrightharpoons}} [Ca_2HCO_3]^{3+} \underset{K_2}{\overset{+Ca^{2+}}{\leftrightharpoons}} \dots} \quad [II]$$

$$\mathrm{\frac{n_{bound}(Ca^{2+})_{bicarbonate}}{n_{bound}(HCO_3^-) + n_{free}(HCO_3^-)} = x_2\frac{K_2{\cdot}c_{free}(Ca^{2+})}{1{+}K_2{\cdot}c_{free}(Ca^{2+})}} \quad [15]$$

where x_2 represents the number of binding sites for Ca^{2+} ions on a HCO_3^- ion and K_2 denotes the microscopic equilibrium constant of calcium bicarbonate. $\mathrm{n_{bound}(Ca^{2+})_{bicarbonate}}$ signifies the amount of Ca^{2+} bound to HCO_3^- ions, which is equivalent to $\mathrm{n_{bound}(HCO_3^-)}$. $\mathrm{n_{bound}(HCO_3^-)}$ (Equation [7]) and $\mathrm{n_{free}(HCO_3^-)}$ (Equation [16]) represent the amount of bound and free HCO_3^- ions, respectively. $\mathrm{c_{free}(Ca^{2+})}$ is the concentration of free Ca^{2+} ions in the system.

$$\mathrm{n_{free}(HCO_3^-, t) = \lambda(HCO_{3,\,aq}^-)_{pH}\left[n_{total}(carbonate, t{=}0) - n_{bound}(Ca^{2+}, t) - n_{outgassing}(CO_2, t)\right]} \quad [16]$$

where $\mathrm{\lambda(HCO_{3,\,aq}^-)_{pH}}$ represents the fractional number of HCO_3^- species.

The microscopic binding parameters x_2 and K_2 are accessible from the average values of $\mathrm{n_{bound}(HCO_3^-, t)}$, $\mathrm{n_{free}(HCO_3^-, t)_{bicarbonate}}$ and $\mathrm{c_{free}(Ca^{2+}, t)}$ which were derived by a linear fit of the data (Figure S8). The macroscopic association constant for the formation of calcium bicarbonate ion pairs in clusters (K_2') can be acquired by multiplying x_2 with K_2[29]. However, the obtained x_2 and K_2 values are negative (Table S4), suggesting that the multiple binding model does not adequately describe the Ca^{2+} and HCO_3^- ion association;

$$\mathrm{Ca_{aq.}^{2+} + HCO_{3,\,aq.}^- \leftrightharpoons [CaHCO_3^+]_{cluster,\,aq.}}$$

$$\mathrm{K_{CaHCO_3^+} = \frac{c([CaHCO_3^+]_{cluster,\,aq.})}{c(Ca_{aq.}^{2+})\cdot c(HCO_{3,\,aq.}^-)} \cong K_2' = x_2 \cdot K_2} \quad [17]$$

where $\mathrm{c(Ca_{aq.}^{2+})}$ and $\mathrm{c(HCO_{3,\,aq.}^-)}$ represent the concentrations of free Ca^{2+} and HCO_3^-, respectively. $\mathrm{c([CaHCO_3^+]_{cluster,\,aq.})}$ indicates the concentration of bound HCO_3^- species.

1.5 Fractions of Bound Ca^{2+}, HCO_3^- and CO_3^{2-} Ions at Distinct pH

Based on the equilibrium constant and the linear development of n_{bound} (Ca^{2+}, t) versus pH (Figure S8), the theoretical relative amount of bound Ca^{2+}, CO_3^{2-} and HCO_3^- at lower pH levels can be predicted. In an empirical method, the slopes of n_{bound} (Ca^{2+}) with time-development are fitted linearly. Further, the acquired pH-development of the n_{bound} (Ca^{2+}, t) facilitates the evaluation of the time-development of n_{bound} (Ca^{2+}, t) at distinct pH values (Figure S8). The ratio of time-development for n_{bound} (Ca^{2+}, t) and n_{added} (Ca^{2+}, t) gives the percentage of total bound Ca^{2+} ions at the particular pH values. The macroscopic equilibrium constant is pH-independent at pH values below 8.5 (Table S3, Table S4). Applying the equilibrium constant of $CaCO_3^0$ and $CaHCO_3^+$ as 1700 and 20 M^{-1}, respectively, the ratio of bound CO_3^{2-} and bound HCO_3^- ions is obtained. The interpolation was conducted within 0.1 pH increments and extrapolated to pH 6.8 (Figure S9).

1.6 Calculation of Ion Products

The temporal evolution of ion products was calculated by using the concentrations of free calcium and free carbonate ions (main article, Figure 3). Since the calibration of the ion-selective electrode was carried out in pure water, the values reflect ion activity products as demonstrated elsewhere[32]. As mentioned above, the CO_2 out-diffusion from the carbonate solution need to be considered. Figure S15 shows the profiles of ion products before and after CO_2 out-diffusion correction.

1.7 TGA and DSC

The stoichiometry of the ACCs prepared at pH 7.5 and pH 8.0 was characterized by TGA (Figure S22, Table S11). The initial weight losses between 30 and 250°C in the TGA profiles might be due to the hydration constituents of ACCs. Subsequently, additional weight losses between 400 and 600°C for samples at pH 8 and 7.5 are found, which can be assigned to the formation of $Ca(OH)_2$ for ACCs synthesized at higher pH.[29,33] However, the corresponding IR spectra do not show any peaks characteristic of $Ca(OH)_2$ (Figure S17) and also the samples were prepared at lower pH levels. Thus, we exclude the possibility that the mass losses are as a result of formation of $Ca(OH)_2$. Additionally, energy dispersive X-ray spectroscopy (EDX) shows that the ACCs contain insignificant impurities of sodium and potassium (atom% below 2%) (Figure S23). Thus, we suppose that the weight losses might be caused by the minor amount of bicarbonate occluded with the ACCs:

$$\mathrm{Ca(HCO_3)_2 \rightarrow CaCO_3 + H_2O + CO_2}\ \ (162\ \mathrm{u} \rightarrow\ 100\ \mathrm{u} + 18\ \mathrm{u} + 44\ \mathrm{u})$$

The mass losses in the later stage between 600 and 850°C arise from the decomposition of calcium carbonate:

$$\mathrm{CaCO_3 \rightarrow CaO + CO_2}\ \ (100\ \mathrm{u} \rightarrow\ 56\ \mathrm{u} + 44\ \mathrm{u})$$

DSC elucidates the thermal transitions of ACCs. Two sets of endothermic reactions, corresponding to the peaks at approximate 100 and 650°C, represent the dehydration of structural water and the decomposition of crystalline $CaCO_3$ into CaO and CO_2, respectively. The endothermic peaks, indicating the crystallization of anhydrous ACCs, of the samples synthesized at pH 7.5 and 8.0 are located at 350 and 359°C, respectively. This suggests that the thermal stability of the sample at pH 8.0 is slightly higher than that at pH 7.5. However, the thermally-induced transitions of both anhydrous ACCs present similar estimated enthalpies (ΔH_{cryst}) for the crystallization (Table S11).

1.8 Analyses of Post-Nucleation Precipitates

In the IR spectra of post-nucleation sediments at given pH values, the characteristic peaks at 1087 cm^{-1} and 1077 cm^{-1} (ν_1), 873 cm^{-1} (ν_2), and 744 cm^{-1} (ν_4) correspond to vaterite. The hydration peak at around 3300 cm^{-1}, however, indicates the co-existence of amorphous minerals in these samples, suggesting a mixture of ACC and vaterite. The hydration peak becomes more apparent at lower pH levels (Figure S24). This is in line with our studies for the ion product of calcium carbonate, in which at all investigated pH values amorphous phases form as the initially precipitated nucleation products. In addition, the hydration band is consistent with the higher solubility of calcium carbonate phases nucleated at a lower pH level, which might be caused by the hydration molecules associated with bicarbonate ions. From cryo-TEM investigations, the co-existence of amorphous structures and vaterite crystals was found in the post-nucleation regime at pH 8.0 and 8.5 (Figure S25). The corresponding SEM images also show vaterite microcrystals accompanied by amorphous nanoparticles. The amorphous nanoscopic particles were more abundant at lower pH levels relative to pH 9.0 (Figure S26), which is consistent with the water peak shown in the IR spectra (Figure S24).

2 Supplementary Discussions

2.1 Ion Association of Calcium Carbonate at Lower pH and the Participation of Bicarbonate

To investigate the ion association tendencies in distinct mineralization solutions maintained at fixed pH values between pH 7.5 and 9.0, we utilized a quantitative potentiometric titration technique, which is based on *in-situ* measurements of free calcium ions by using a calcium ion-selective electrode at constant pH. As discussed in detail, this enables the quantitative analysis of ion association at the different stages of mineral nucleation (pre-nucleation, nucleation and post-nucleation).[29]

During a titration experiment, a dilute calcium chloride ($CaCl_2$) solution is slowly and continually titrated into a dilute carbonate buffer (see the experimental section) at a fixed pH value, which allows supersaturation to slowly evolve and subsequently reach a critical point, resulting in the nucleation and precipitation of mineral ($CaCO_3$) particles (Figure S1).The deficit in the detected free Ca^{2+} ions when compared to the added amount represents the formation of stable ion associates through the binding of Ca^{2+} ions and carbonate species.[29] While the experimental proof of PNCs relies on the detection of entities significantly larger than ion pairs by analytical ultracentrifugation and was previously presented for pH values larger than 9.0[29], there is, in our opinion, no reason to assume that they do not exist at lower pH (see below). In any case, the linear development of free Ca^{2+} ions with time shows that ion association occurs in the undersaturated and supersaturated stages. For titrations conducted using $CaCl_2$ solutions (10 mM) dosed into carbonate butter (10 mM), approximate 38%, 30%, and 20% of dosed calcium ions are bound at pH 9.0, 8.5, and 8.2, respectively, in the pre-nucleation regime (Figure S2A). When the pH value is maintained below 8.0, no apparent nucleation is observed at the investigated concentrations of mother solutions for the duration of the experiments. To quantitatively evaluate ion association at lower pH levels, increased concentrations (20 mM) of $CaCl_2$ solution and carbonate buffer were applied. At pH 8.5, 8.2, 8.0, and 7.8, around 45%, 38%, 36%, and 25% of added calcium ions are in a bound state, respectively (Figure S2B). Under the conditions utilized, no nucleation occurs at pH values below 7.6. From the titration curves (Figure S2), it is observed that, as the pH level decreases, the ratio of bound Ca^{2+} ions to the counter ions declines. In light of the reported association between Ca^{2+} ions and CO_3^{2-} ions in the pH range between 9.0 and 10.0,[29] the observed trend can be attributed to the decreasing fraction of CO_3^{2-} ions in buffer solutions maintained at low pH (Table S1). At conditions of pH 8.0, 8.2, 8.5, and 9.0, the respective fraction of CO_3^{2-} ions in the buffer solutions is rather low, corresponding to 0.46 %, 0.73%, 1.45%, and 4.5%, respectively (Table S1). Thus, the pH-dependent speciation of CO_2, HCO_3^-, and CO_3^{2-} in carbonate buffer, which influences the supersaturation level of the solution, affects the fractions of bound Ca^{2+} ions and related pre-nucleation equilibria (Figure S2). In addition, as the pH levels go down, the fraction of CO_2 starts to increase (Table S1) and correspondingly influences the acid/base counter titration necessary to maintain a constant pH. In the pre-nucleation regime at pH values below 8.5, HCl addition is required to balance the out-diffusion of CO_2 (SI Results and Discussion section 1.1, Figure S3, Figure S4). Since the fraction of CO_3^{2-} ions in the carbonate buffer is extremely low at pH values below 8.0 (Table S1) and the out-diffusion of CO_2 becomes more and more pronounced at lower pH values (Figure S6), the investigated pH range confronts a lower limit when it comes to a fully quantitative evaluation of the pre-nucleation ion association (see below).

During the course of the titration experiments, the pH conditions are kept constant by the addition of NaOH and HCl solutions, enabling the quantitation of bound carbonate species (SI Results and Discussion section 1.1). Previous studies have shown that in the range of pH 9.0–10.0, Ca^{2+} ions bind CO_3^{2-} ions in an equimolar ratio, which was corroborated by potentiometric titration[29] and conductivity measurements[30]. In this pH regime, the amount of bound Ca^{2+} and bound CO_3^{2-} ions, assessed by the potential of Ca^{2+} and the volume of added NaOH respectively, overlay completely (Figure S7A), showing that Ca^{2+} and HCO_3^- ion association is insignificant above pH 9.0.[29,30] However, at pH below 8.5, the decreasing fraction of CO_3^{2-} ions in the buffer (Table S1) raises the importance of HCO_3^- species in ion association behavior during the pre-nucleation regime. For instance, at pH 8.5, after correcting for CO_2 outgassing, the amount of bound Ca^{2+} ions is considerably larger than the amount of bound CO_3^{2-} ions (Figure S7B). Since there is no reason to assume that the equimolar binding ratio between Ca^{2+} ions and CO_3^{2-} ions is affected by the decreasing pH values from 9.0 to 8.5, wherein the fraction of CO_3^{2-} in the buffer decreases from 4.5% to 1.5% (Table S1), this suggests that HCO_3^- ions start to play an important role in the overall ion association below ca. pH 8.5. (Figure S7B). In experiments performed at even lower pH conditions (pH 8.2 and 8.0), the differences between total amounts of bound Ca^{2+} ions and bound CO_3^{2-} ions become even larger (Figure S7C, D), due to a continually decreasing carbonate fraction.

Descriptions of calcium carbonate ($CaCO_3^0$) and calcium bicarbonate ($CaHCO_3^+$) ion pairs in solution were first reported by Greenwald.[34] Regarding the respective equilibrium constants, a considerable disparity exists in the literature.[35–37] However, there is a consistent trend that the interactions of Ca^{2+} with CO_3^{2-} ions are stronger than those with HCO_3^- ions, with reported equilibrium constants being in the range of 1000–2000 M^{-1} and 10–20 M^{-1}, respectively. Based on this, our titration data are consistent with the literature, showing that the equilibrium constant of $CaCO_3^0$ ion pair formation is approximately 100-fold higher than that of $CaHCO_3^+$ at lower pH levels (Table S2), whereas they are independent of pH to within experimental accuracy in this pH regime. The association constants of $CaCO_3^0$ and $CaHCO_3^+$ (Table S2) correspond to standard Gibbs free energies of -18.43 and -7.42 kJ/mol for the formation of $CaCO_3^0$ and $CaHCO_3^+$, respectively. This shows that although the calcium bicarbonate interaction is considerably weaker than for calcium carbonate, it can still play a critical role during mineral pre-nucleation stages at near-neutral pH. Note that although at lower pH, the calcium bound fraction of HCO_3^- ions is dominant relative to the bound fraction of CO_3^{2-} ions, the calcium carbonate interactions cannot be considered insignificant and also contribute to ion association.

At pH 8.5, the ratio of calcium bound HCO_3^- ions and bound CO_3^{2-} ions in the pre-nucleation stages is approximately 1.0, which reflects that the total amount of calcium (bi)carbonate ion associates is constituted of equal proportions of Ca^{2+} ion bound CO_3^{2-} and HCO_3^- ions. At pH 8.2 and 8.0, the ratio is ca. 1.4 and 2.7, respectively (Table S2), indicating that the ion associates contain larger fractions of HCO_3^- ions. Based on the equilibrium constants and empirical pH-development of bound Ca^{2+} ions (Figure S8), the theoretical percentage of bound Ca^{2+} ions categorized into fractions bound to HCO_3^- ions and CO_3^{2-} ions are accessible at distinct pH conditions (Figure S9). According to this extrapolation, at pH values below 7.1, in the pre-nucleation stage, the ion association is insignificant wherein the percentage of bound Ca^{2+} ions is 2.1% at pH 7.1 and becomes negligible at lower pH. This represents the lower limit of pH essential for $CaCO_3$ based mineralization reactions in a homogenous environment.

2.2 Calculation of the Stability of Bicarbonate Species in Aqueous Solution and Their Acidity

In order to confirm the experimental finding that multiple binding equilibria for bicarbonate are not required, we have computed the stability of bicarbonate species in aqueous solution based on the use of polarizable force field-based molecular dynamics to determine the equilibrium constants and thus the standard free energy for the possible association processes (Table S5). First of all, the calculated free energy for the formation of $CaHCO_3^+$ is computed to be -7.8 kJ/mol, which corresponds to an equilibrium constant of 23.2 M^{-1} in good agreement with the reported experimental range of values. Similarly, the ion pairing for $CaCO_3^0$ has a free energy of -17.3 kJ/mol at 300 K,[5] which is also close to experimental estimates (-18.0/-19.0 kJ/mol[30,38]). The temperature dependence of the $CaHCO_3^+$ binding free energy (Figure S10) is also consistent with the experimental estimates (Table S5), confirming the reliability of the computational model used in this work.

It should be noted that the current polarizable model corrects the over-binding exhibited by our previous rigid ion force field.[30] The addition of a further bicarbonate to $CaHCO_3^+$ is still exergonic (-2.9 kJ/mol), but with a reduced free energy, which implies that this species would spontaneously react with any free $Ca^{2+}_{(aq)}$ to form two ion pairs. The addition of a third bicarbonate to a single calcium ion is instead unfavorable (+3.3 kJ/mol) and so can be ruled out as a likely process unless bicarbonate is in substantial excess.

The binding of bicarbonate to either one or two calcium ions has also been considered as this can provide insight regarding the change in acidity as a function of the calcium coordination number. Using a simple thermodynamic cycle (Figure S12), it is possible to use the association free energies to compute the shift of bicarbonate pK_a based on the experimental value for isolated bicarbonate in water (Table S6, Table S7). Ion pairing reduces the bicarbonate pK_a from 10.3 to 8.6. In the case where two or three HCO_3^- ions coordinate to the same calcium ion then the pK_a values increase with the number of bound bicarbonates, but only slightly, suggesting that the coordination to calcium is the dominant influence rather than other possible factors, such as the overall cluster charge. If bicarbonate bridges between two calcium ions then the pK_a again falls to 6.6, which implies that under the pH conditions of the present experiments this bicarbonate would be deprotonated. From this, a picture emerges that is consistent with previous observations of calcium carbonate/bicarbonate clusters (DOLLOPs) in which carbonate acts as the bridging ion in the polymer-like structures, while bicarbonate appears to bind only as a chain-terminator.[3] If the observed quantitative trend of lowering the pK_a by ~1-2 units per calcium coordinated to bicarbonate continues to higher values, this implies that bicarbonate should largely be absent from the surface sites of crystalline mineral phases, such as calcite. We note that a similar trend has been proposed by Andersson and Stipp for adsorbed water on calcite surfaces.[39]

In order to further validate the above free energy calculations for the shift in the bicarbonate pK_a we have also used *ab initio* quantum mechanical methods to determine this quantity for the $CaHCO_3^+$ ion pair. Here, the deprotonation energy of bicarbonate to carbonate was computed using a combination of explicit water embedded within a continuum dielectric. Note that here we again use the change in acidity relative to the experimental value for bicarbonate rather than attempting to determine directly the absolute value, which has been shown to be particularly challenging even at this level of theory. Runs were performed as a function of the number of explicit water molecules included to examine the effect on the pK_a shift. As anticipated, based on previous studies of acidity, unless the first solvation shell of all ions is almost all explicitly represented then the error was often large (e.g., for a pure continuum model the shift was ~10 larger than for the most accurate case). Using results for deprotonation of $HCO_3(H_2O)_6^-$ as the reference, and with $CaHCO_3(H_2O)_7^+$ for the ion pair, the pK_a is predicted to shift from 10.3 to 8.4 on binding the first calcium ion, which is in excellent agreement with the force field-based free energy results. Similarly, for bicarbonate bridging between two calcium ions with an explicit first solvent shell ($Ca_2HCO_3(H_2O)_{11}^{3+}$) the pK_a is estimated to fall to 7.2; only slightly higher than the force field value of 6.6.

2.3 Comparison of Calculated and Experimental Chemical Shifts

To benchmark the quantum mechanical method employed here for solid-state calculations, we have first examined a range of crystalline phases of calcium/sodium carbonate/bicarbonate, with and without water of hydration present. Specifically, we have performed calculations for calcite ($CaCO_3$), monohydrocalcite ($CaCO_3.H_2O$), ikaite ($CaCO_3.6H_2O$), nahcolite ($NaHCO_3$), trona ($Na_3(CO_3)(HCO_3)(H_2O)_2$), wegscheiderite ($Na_5(CO_3)(HCO_3)_3$), and models for both dry and wet ACC. The optimized lattice parameters for the crystalline phases are given in Table S8. With the exception of nahcolite, all values are reproduced to better than 2%, while the majority of cell parameters are within 1%. The use of the alternative dispersion corrections of Tkatchenko-Scheffler was also explored, though this led to larger errors in the lattice parameters of up to almost 6% in the case of nahcolite. For the dry and wet forms of ACC, the final densities are 2.69 and 2.41 g/cm^3, respectively, where the latter value compares well to the reported value of Goodwin *et al.* of 2.43 g/cm^3 for a similar level of water content[21].

Computed ^1H and ^{13}C chemical shifts for the crystalline phases are given in Table S9 based on the use of nahcolite as the point of reference. Unfortunately, experimental values are not available in the literature for all of the above minerals, but some validation is possible in the case of monohydrocalcite. Here, both the proton and carbon chemical shifts are reproduced to within the line width, despite the fact that the values are very different, being for water and carbonate in monohydrocalcite, respectively, as opposed to bicarbonate in nahcolite. Similarly, the ^{13}C chemical shift for calcite is reproduced to within 0.5 ppm. In the case of the complex mineral trona, which features a proton disordered over two sites between an especially short carbonate-carbonate distance, only this unusually high ^{1}H chemical shift has been reported. While the calculated chemical shift for this case shows a higher discrepancy than for the other systems, most likely due to the need to use an ordered proton distribution, the trend is still clearly evident.

For amorphous calcium carbonate, both anhydrous (dry) and hydrated (wet) models have been created, where the hydrous model has a water to calcium carbonate ratio of 1, in line with the approximate composition of the experimental samples. Chemical shifts have been computed for the as-created model with pure carbonate, as well as for configurations that contain bicarbonate defects. Here, bicarbonate is incorporated either via substitution for carbonate at a concentration of 2.7% or for wet ACC via a double bicarbonate substitution associated with a Ca^{2+} vacancy to charge-compensate. Results for all amorphous systems are given in Table S10.

Starting with the pure carbonate case, the average ^{13}C chemical shift is 167.20 and 167.94 ppm for dry and wet ACC, respectively. This is remarkably consistent with the value of 167.98 ppm reported by Nebel *et al.*[40] for an ACC sample with a water content of 0.473 per formula unit. It should be noted that the experimental line width is similar to the range of values found within the amorphous structures. On replacing one carbonate anion by bicarbonate, a range of possible chemical shifts is found for both nuclei associated with the introduced HCO_3^-. For the ^{1}H values, these broadly follow the expected correlation with the hydrogen bond length of the bicarbonate proton. Some defect configurations suggest that the ^{13}C of bicarbonate in ACC could be strongly shielded, which is inconsistent with the reported HETCOR data. However, when the relative energies of the structures are computed, the most stable structures for both wet and dry ACC have chemical shifts closer to the expected range. This is also true for the double substitution combined with a calcium vacancy. For the single bicarbonate substitution in wet ACC, the four configurations chosen represent different environments within the structure based on the heterogeneous water distribution. The least stable structure has bicarbonate hydrogen bonding to a water molecule, while the two intermediate configurations are situated within the dry region, though with some proximity of water to bicarbonate but primarily on the opposite side to the hydroxyl group. The most stable location for bicarbonate lies at the interfacial region between the drier region and water, but where the bicarbonate remains hydrogen bonded to a carbonate anion that is also at this interface. Although caution should be exercised in drawing conclusions from a small sample of configurations (due to the cost of the quantum mechanical calculations), this result is at least consistent with a hypothesis that bicarbonate preferentially associates with the surface of droplets as they dehydrate toward ACC.

2.4 Hydrogen Bond Network between Bicarbonate ions and Carbonate ions

In $^{13}C\{^{1}H\}$ 2D HETCOR NMR at pH 7.5, the skew of the bicarbonate signal reflects the variation in both the ^{13}C and ^{1}H chemical shifts as the chemical environment of the acidic proton of the bicarbonate varies (Figure 5, main text). The ^{1}H chemical shifts of acidic protons involved in the hydrogen bond network will be shifted in the deshielded direction, depending on the extent of the hydrogen bonding strength.[41] If bicarbonate ions are incorporated into a matrix of carbonate ions, it is conceivable that intermolecular hydrogen bonding occurs between the bicarbonate ions and their neighboring carbonate ions. The observation of a skew indicates that there is a continuous distribution of such hydrogen bonding strengths. The same extent of the skewness is also observed for the HETCOR of the samples prepared at pH 8.0 and 8.5 (Figure S19, Figure S20). Nonetheless, it is impossible to quantify the distribution because the signal intensity also depends on the transfer efficiency during the signal transfer.

In addition, Figure S21 shows the trend of the merging of the carbonate and bicarbonate peaks. It has been shown that the ^{1}H chemical shift of an acidic proton of the moieties such as bicarbonate or water would increase with acidity. Thus, the merging of the two components correlates well with the increase in the proton chemical shift. The relatively large line width (> 7 ppm) of the peak for 17 ppm (^{1}H dimension) indicates that the peak comprises two components. Although their exact chemical shifts cannot be determined unequivocally, the center of gravity of each peak is midway between the chemical shifts of carbonate and bicarbonate. This observation is consistent with the structural scenario that the acidic protons of some bicarbonate ions are hydrogen-bonded to the neighboring carbonate ions. This intimate interaction between carbonate and bicarbonate may be the clue to bicarbonate incorporation in ACC.

Figures

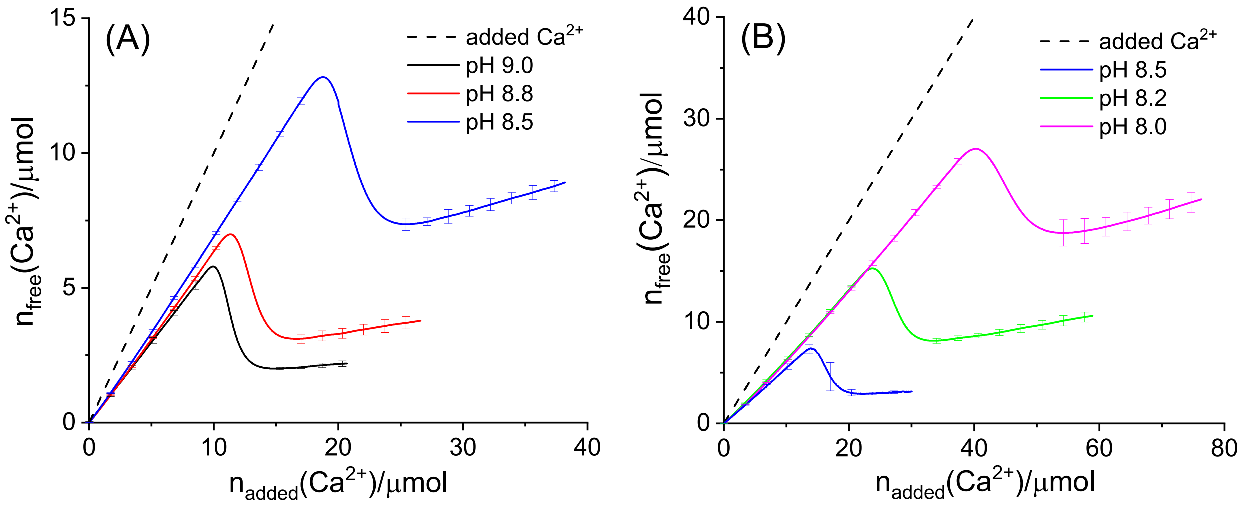

Figure S1. Development of the amount of free Ca^{2+} ions for titrations performed at (A) pH 9.0, 8.8, and 8.5 ($CaCl_2$ (10 mM) titrated into carbonate buffer) and (B) pH 8.5, 8.2, and 8.0 ($CaCl_2$ (20 mM) added into carbonate buffer). The black dashed line represents the amount of total dosed Ca^{2+} ions. Differences between the added and detected calcium thus allow the determination of bound calcium at all stages of the experiments. The average values were based on three independent measurements. Error bars represent ± 1-σ-standard deviation.

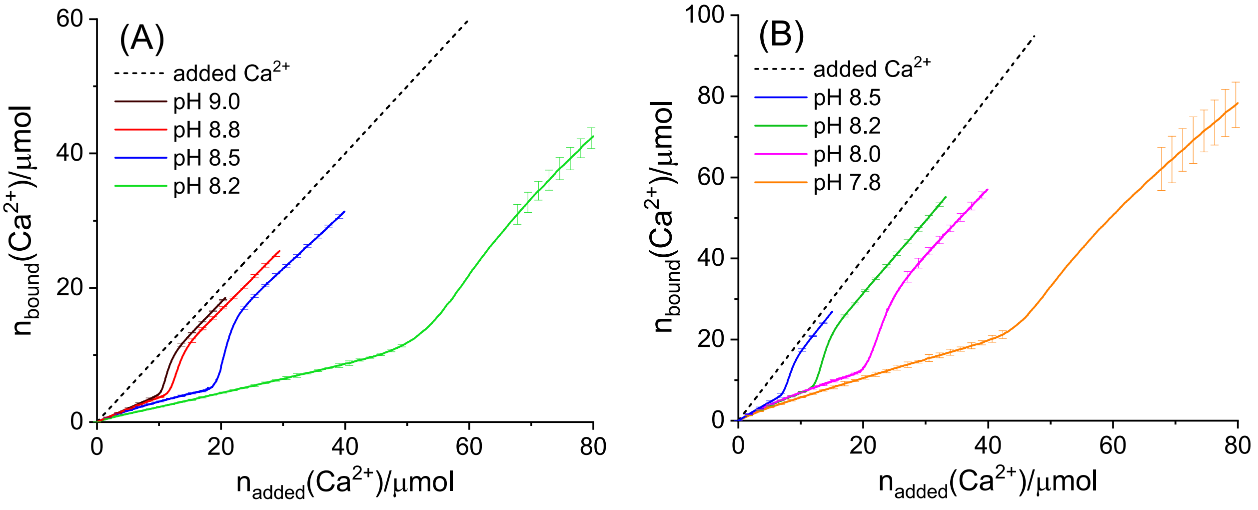

Figure S2. Profile of the amount of bound Ca^{2+} ions at different pH values for titration runs involving (A) $CaCl_2$ (10 mM) dosed into carbonate buffer (10 mM) at pH 9.0, 8.8, 8.5, and 8.2 (B) $CaCl_2$ (20 mM) added into carbonate buffer (20 mM) at pH 8.5, 8.2, 8.0, and 7.8. The average amounts of bound Ca^{2+} ions are assessed from respective differences between the amount of dosed and detected free Ca^{2+} ions. The dashed black line represents a hypothetical scenario involving a complete (100 %) binding of added Ca^{2+} ions. The error bars represent ±1-σ-standard deviation for N = 3 repetitions.

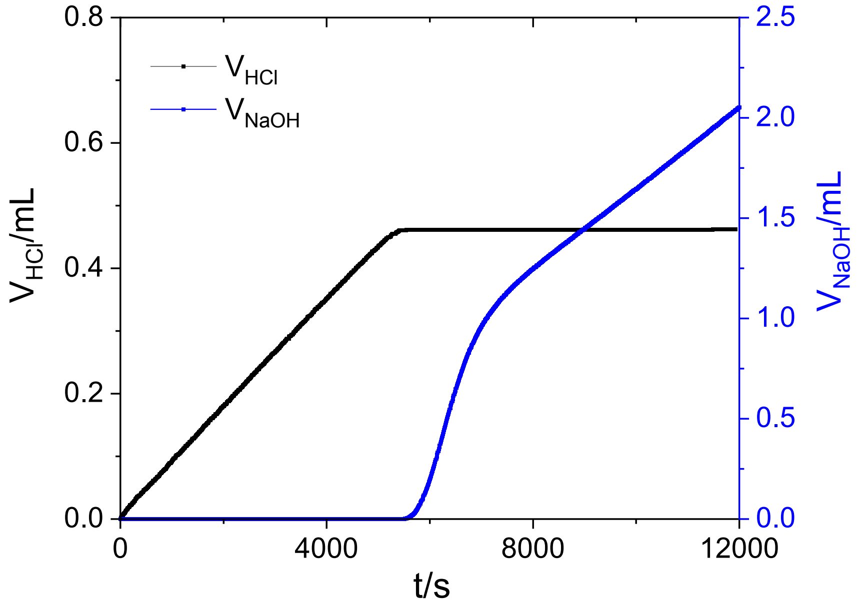

Figure S3. Time-development of HCl (black) and NaOH (blue) addition for titration experiments performed at pH 8.5.

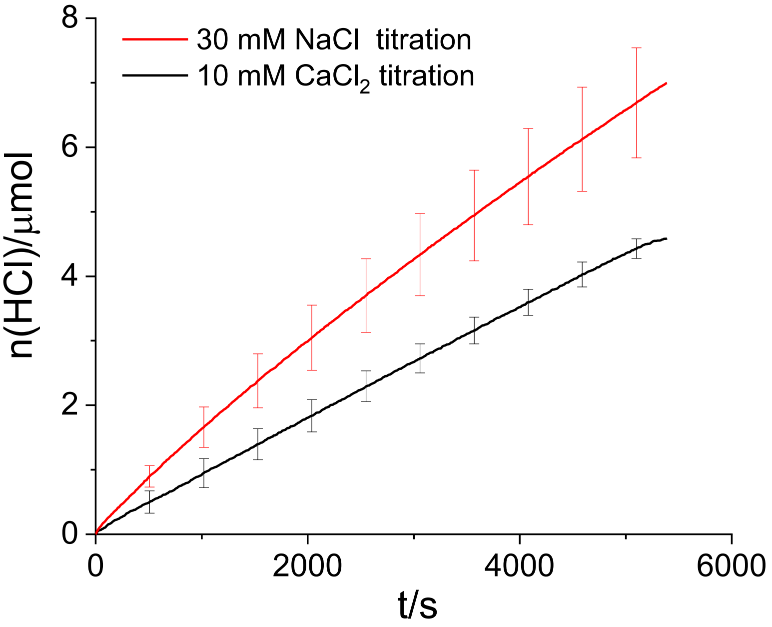

Figure S4. The amount of HCl addition in titration experiments dosing NaCl (red) and $CaCl_2$ (black) solutions into carbonate buffer at pH 8.5.

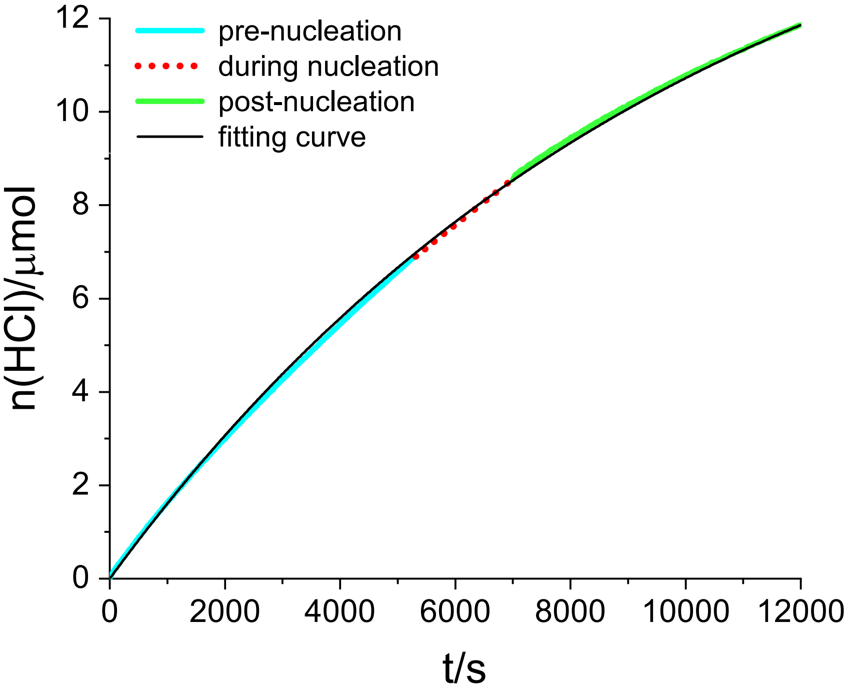

Figure S5. Temporal development of HCl addition for balancing CO_2 out-diffusion in carbonate buffers at pH 8.5, which fits well to an exponential growth function (black line) described as:

$$n_{outgassing}(CO_2, t) = -1.28 \times 10^{-4} \times \exp(-t/11736.5) + 1.28 \times 10^{-4}$$

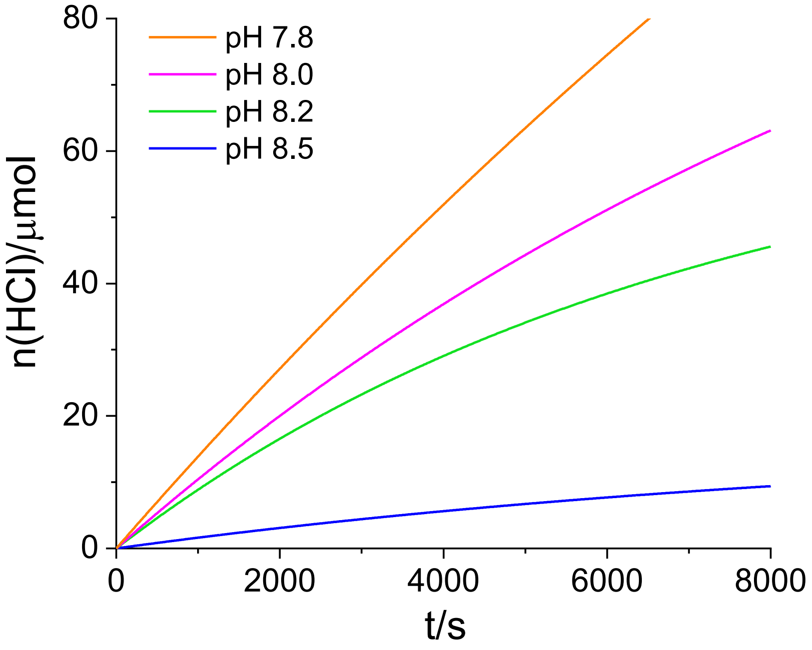

Figure S6. Time development of the amount of HCl required for balancing CO_2 out-diffusion at particular pH values. Here only the fitted curves are shown.

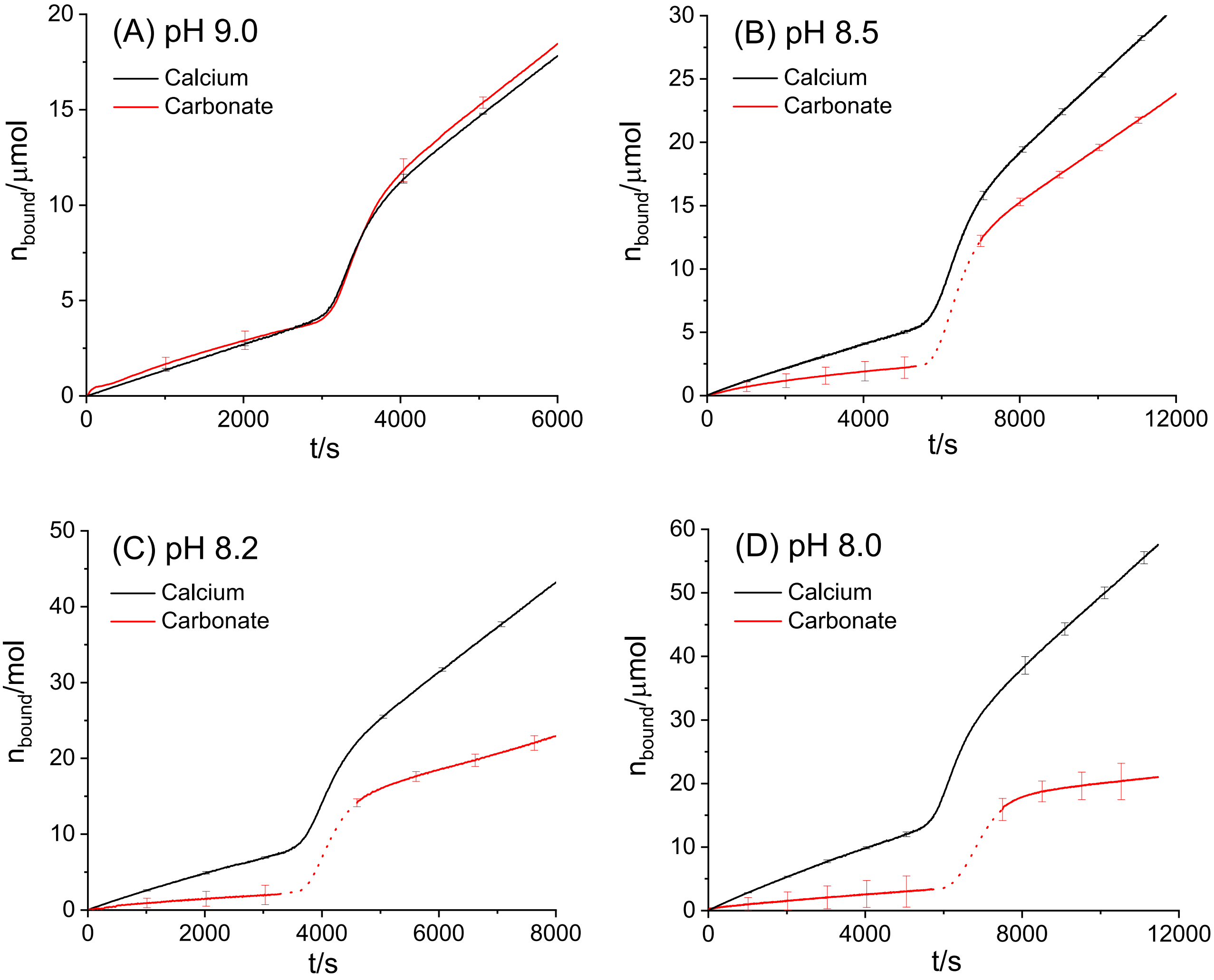

Figure S7. Time evolution of bound Ca^{2+} and bound CO_3^{2-} (black lines and red lines) at (A) pH 9.0 and (B) pH 8.5 ($CaCl_2$ (10 mM) titrated into carbonate buffer (10 mM)) as well as (C) pH 8.2 and (D) pH 8.0 ($CaCl_2$ (20 mM) dosed into carbonate buffer (20 mM)). The data shown is based on the average of three independent measurements. Error bars represent ±1-σ-standard deviation (N = 3).

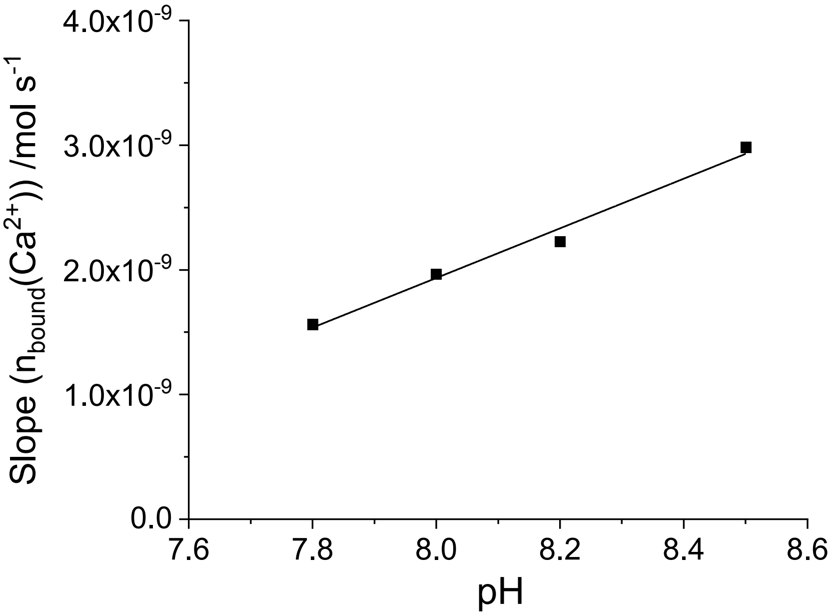

Figure S8. Empirical plot of the slopes of the amount of bound Ca^{2+} ions versus pH. The data points are fitted linearly (R^2 = 0.985).

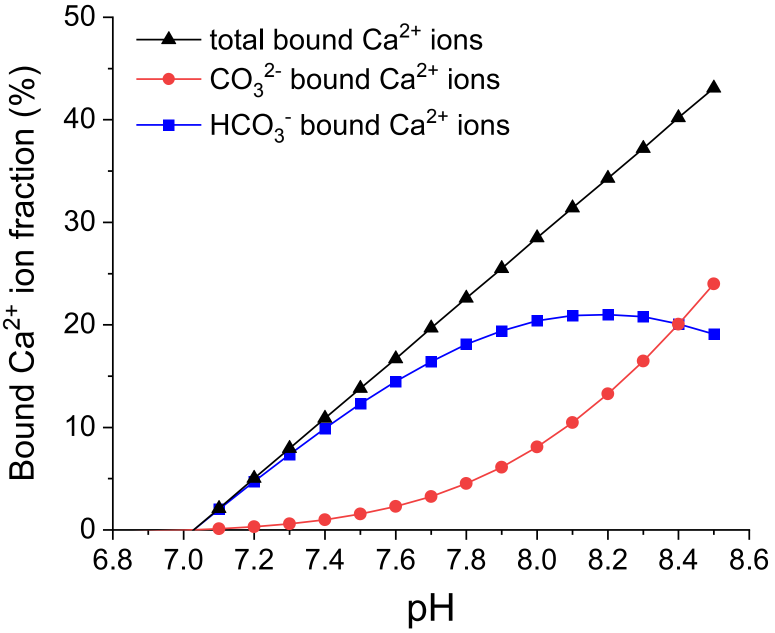

Figure S9. pH-development of total bound Ca^{2+} ion fraction (black), CO_3^{2-} bound Ca^{2+} ions (red), and HCO_3^- bound Ca^{2+} ions (blue).

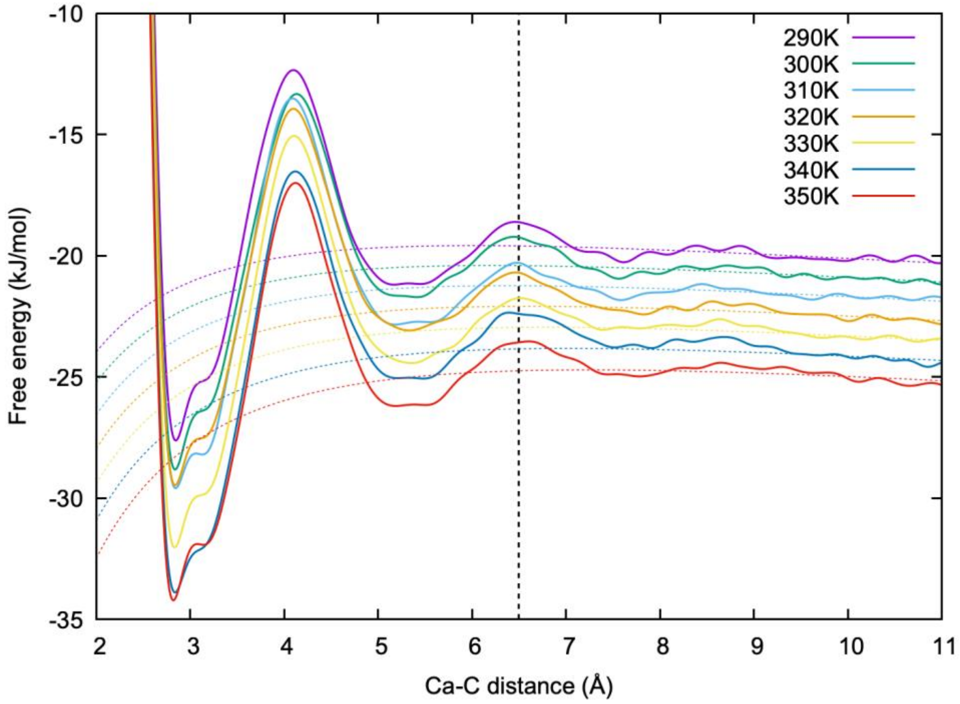

Figure S10. Calcium-bicarbonate ion pairing free energy as a function of temperature computed with the AMOEBA polarizable force field developed in this work. The dashed lines are the analytic solutions used to align the curves for the calculation of the association constant and to verify the convergence of the calculations in the long-range limit.

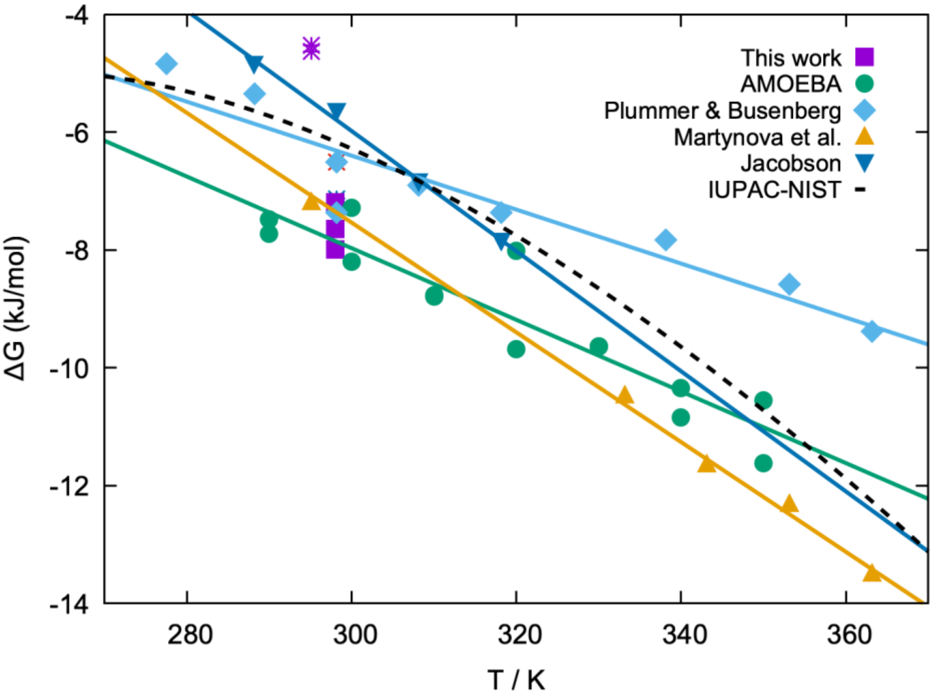

Figure S11. Calcium-bicarbonate association free energy as a function of temperature computed with the AMOEBA polarizable force field developed in this work compared to the experimental estimates from this work (purple squares) and literature values reported in Ref[38]. Filled symbols represent data points (with two independent values per temperature for the simulations in some cases), while lines of the same color represent the corresponding best linear fit.

$$\begin{tikzcd}
2\,\mathrm{Ca}^{2+} + \mathrm{HCO}_3^- \arrow[r, "58.8\ \mathrm{kJ/mol}"] \arrow[d, "-7.8\ \mathrm{kJ/mol}"'] & 2\,\mathrm{Ca}^{2+} + \mathrm{CO}_3^{=} + \mathrm{H}^+ \arrow[d, "-17.3\ \mathrm{kJ/mol}"] \\
\mathrm{CaHCO}_3^+ + \mathrm{Ca}^{2+} \arrow[r, "49.3\ \mathrm{kJ/mol}"] \arrow[d, "+2.4\ \mathrm{kJ/mol}"'] & \mathrm{Ca}^{2+} + \mathrm{CaCO}_3 + \mathrm{H}^+ \arrow[d, "-9.2\ \mathrm{kJ/mol}"] \\
\mathrm{CaHCO}_3\mathrm{Ca}^{3+} \arrow[r, "37.5\ \mathrm{kJ/mol}"] & \mathrm{CaCO}_3\mathrm{Ca}^{2+} + \mathrm{H}^+
\end{tikzcd}$$

Figure S12. Schematic diagram illustrating the thermodynamic cycles used to estimate the acidity of the various calcium bicarbonate clusters based on the experimental bicarbonate pK_a (10.3) and the pairing free energies computed using well-tempered metadynamics and the AMOEBA polarizable force field developed in this work.

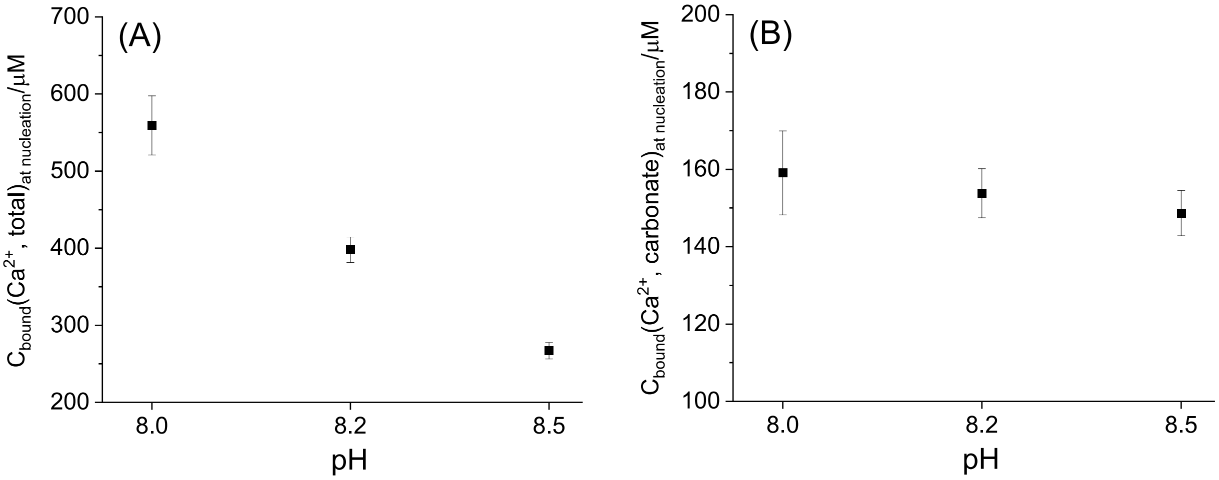

Figure S13. pH-development of the concentration of (A) total bound calcium ions and (B) carbonate bound calcium ions at the nucleation point. At the point of nucleation, the calcium ions bound to carbonate ions show constant levels at distinct pH values within experimental accuracy. The average values and error bars (± 1-σ-standard deviation) were assessed from three independent measurements.

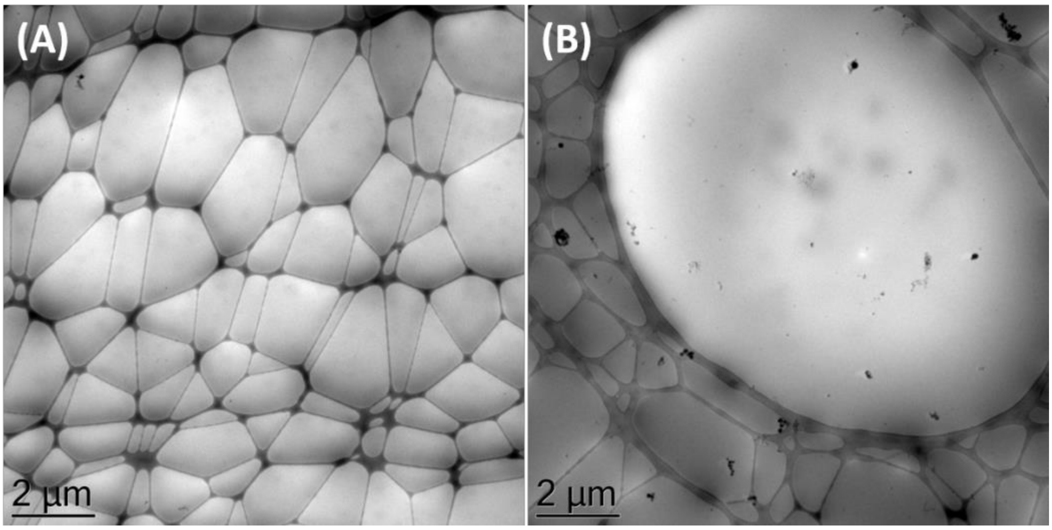

Figure S14. Cryo-TEM overviews for specimens at (A) pH 8.5 (B) pH 8.0. The liquid-like dense phases are distributed over the grids.

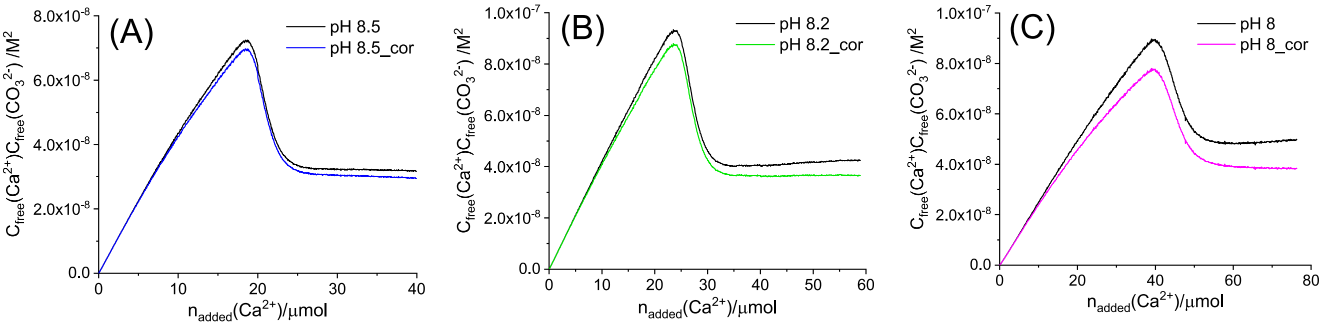

Figure S15. Black and colored lines represent the time-development of ion products for titration performed at (A) pH 8.5, (B) pH 8.2 and (C) pH 8.0 without and with CO_2 out-diffusion correction, respectively.

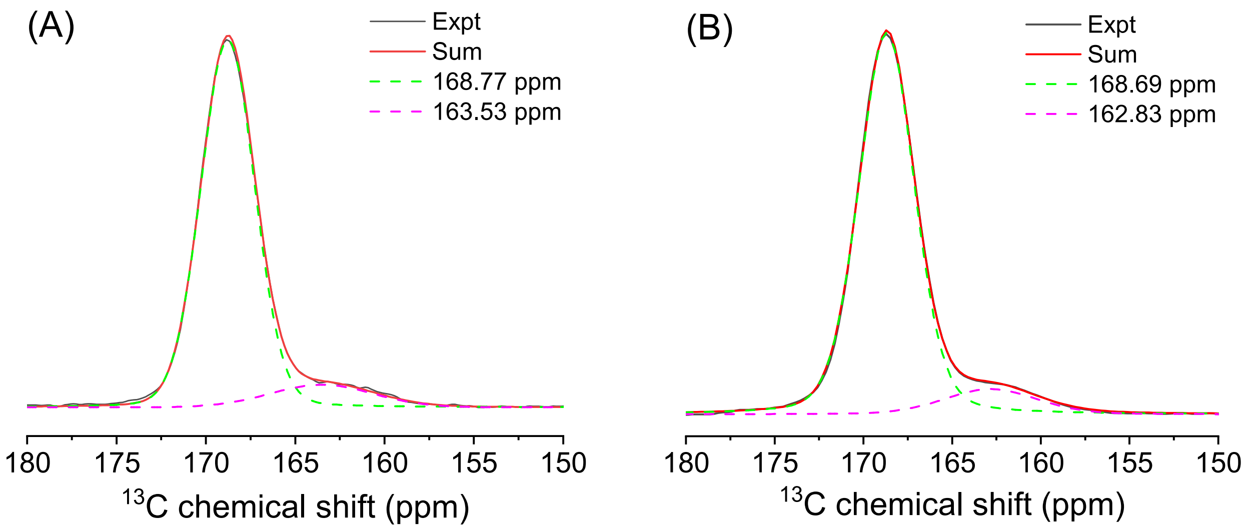

Figure S16. $^{13}C\{^1H\}$ CPMAS spectra for samples prepared at (A) pH 8.5 and (B) pH 8.0 (black solid lines). The spectra were deconvoluted to two spectral components, corresponding to the chemical shifts of proto-calcite ACC (green dashed line) and bicarbonate (pink dashed line), respectively. The red solid lines represent the sum of two deconvoluted peaks.

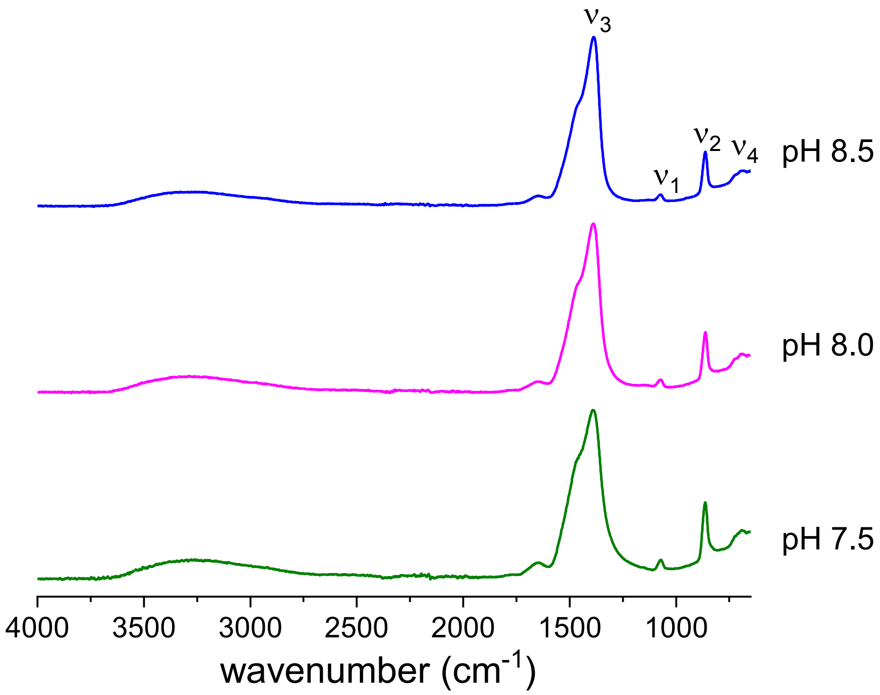

Figure S17. Representative FT-IR spectra of ACCs synthesized at pH 8.5, 8.0, and 7.5. The exact band positions are listed in the main text.

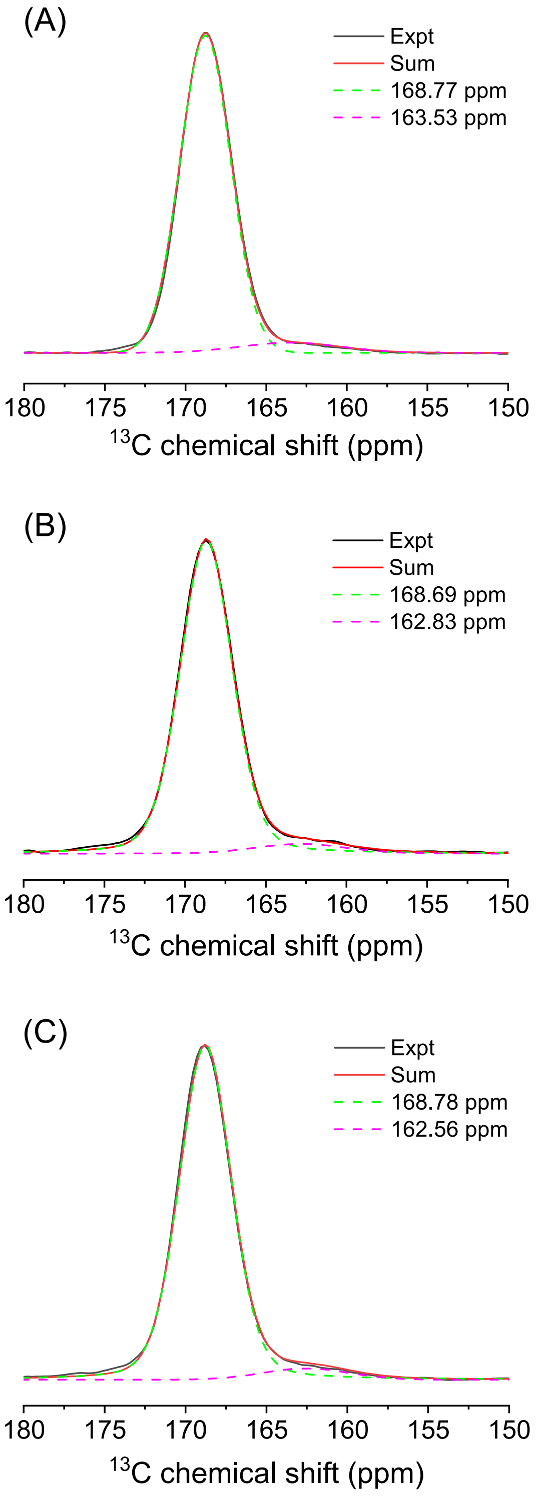

Figure S18. ^{13}C MAS spectra acquired for samples prepared at (A) pH 8.5, (B) pH 8.0, and (C) pH 7.5 (black solid lines). The spectral components were determined based on the ^{13}C{^{1}H} CPMAS spectra.

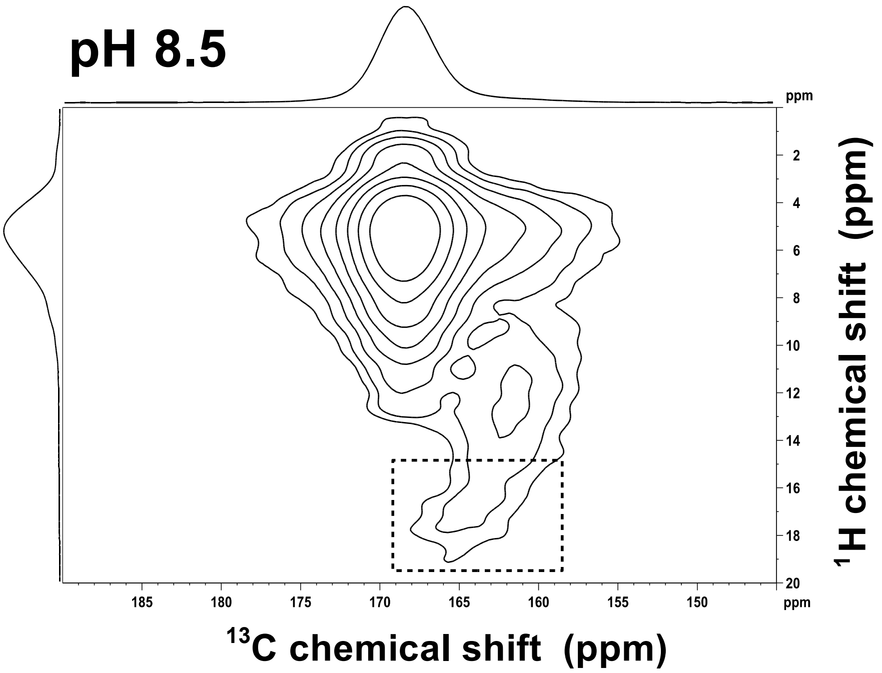

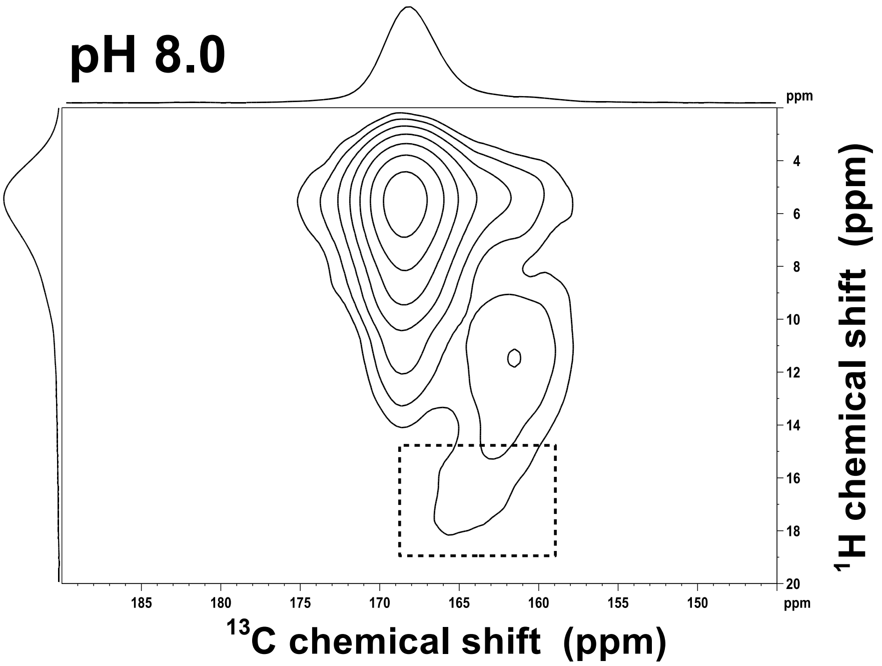

Figure S19. ^{13}C{^{1}H} FSLG-HETCOR spectra acquired for ACCs at pH 8.5 and 8.0. The correlation peaks at approximately 17.5 and 165 ppm of the ^{1}H and ^{13}C dimensions in the dashed frame indicate the bicarbonate species in the vicinity of calcium carbonate.

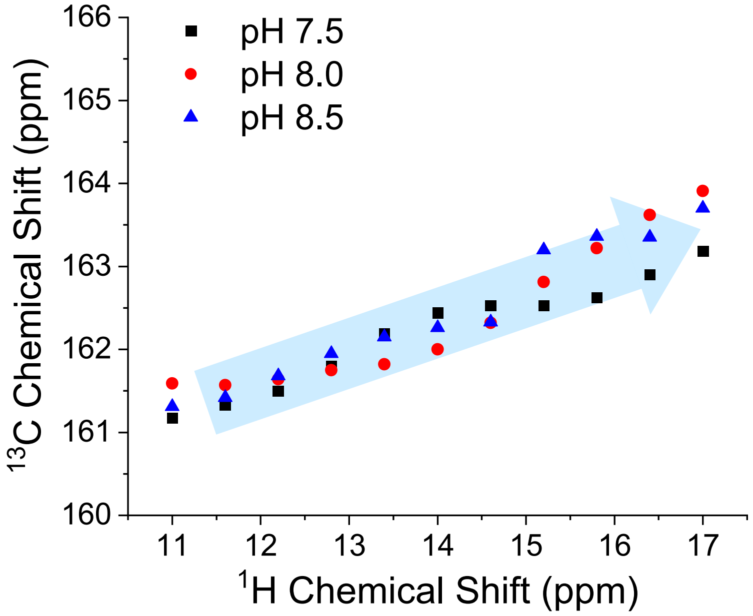

Figure S20. Development of ^{13}C chemical shift of bicarbonate species in the range of 11 and 17 ppm in the ^{1}H dimension based on HETCOR spectra of ACCs prepared at pH 7.5 (black square), 8.0 (red circle), and 8.5 (blue triangle).

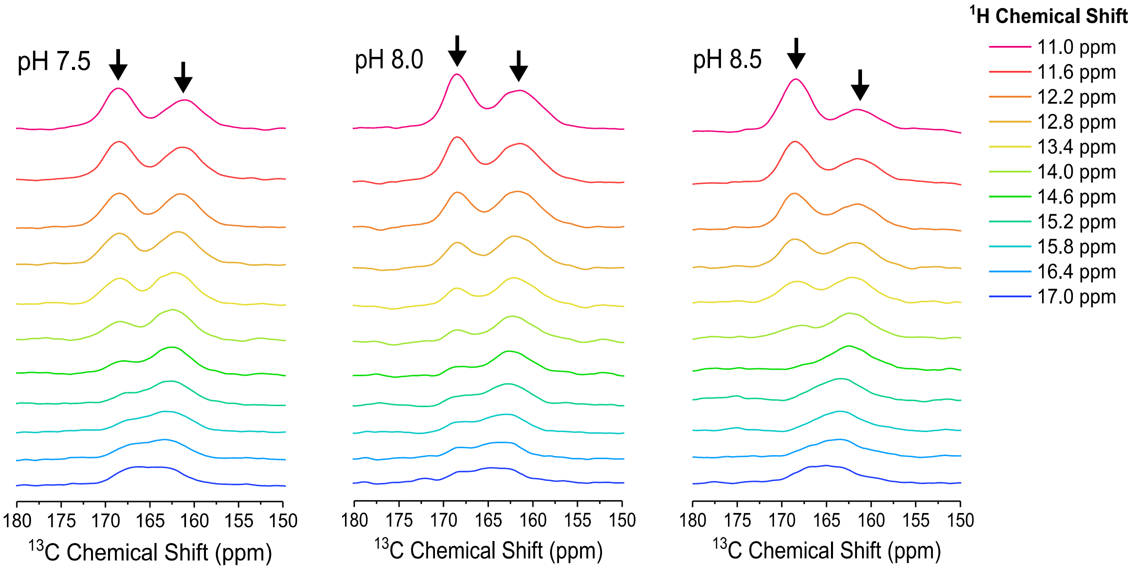

Figure S21. Development of carbonate and bicarbonate species in ^{13}C spectra extracted from HETCOR spectra of ACCs prepared at pH 7.5, 8.0, and 8.5 in the range of 11 and 17 ppm in the ^{1}H dimension. Arrows indicate the carbonate (left) and bicarbonate (right) signals, respectively.

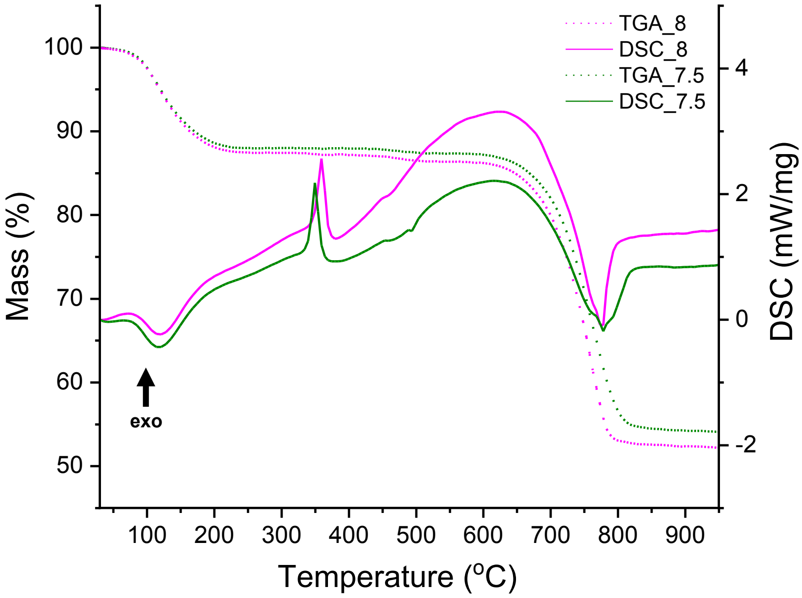

Figure S22. Simultaneous thermal analysis (dotted line) and DSC profiles (continuous line) for amorphous mineral samples prepared at pH 8.0 (pink) and 7.5 (green).

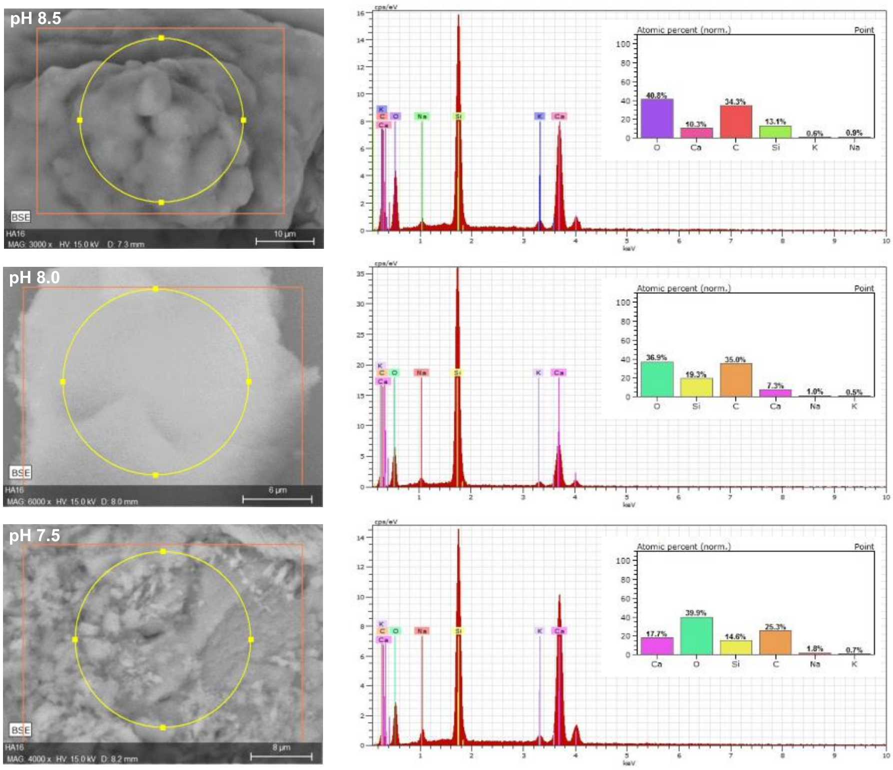

Figure S23. Respective SEM images (left) and EDX spectra (right) of ACCs collected at pH 8.5, 8.0 and 7.5. Atomic percentage (right, normalized values within each measurement) of ACCs was measured from the area in the yellow circle.

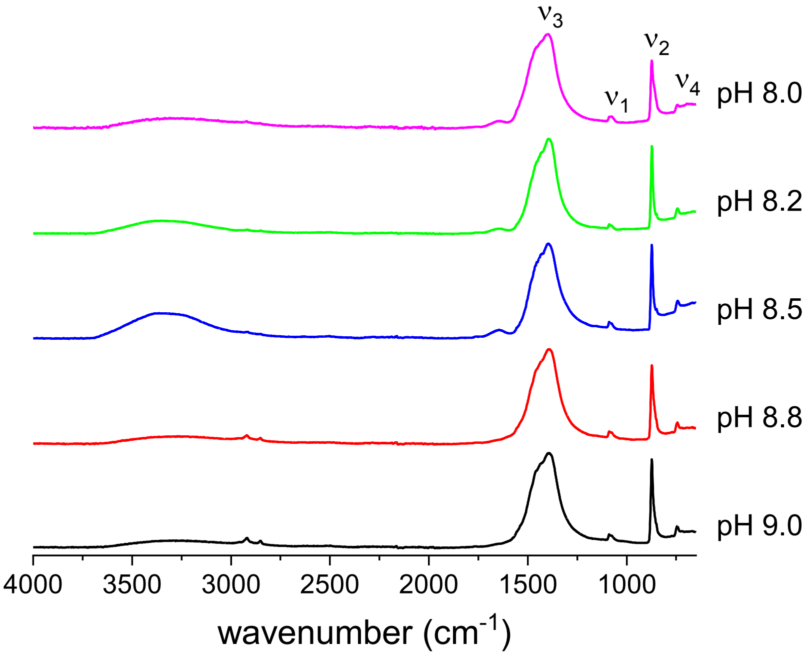

Figure S24. IR spectra of post-nucleation sediments collected at distinct pH levels.

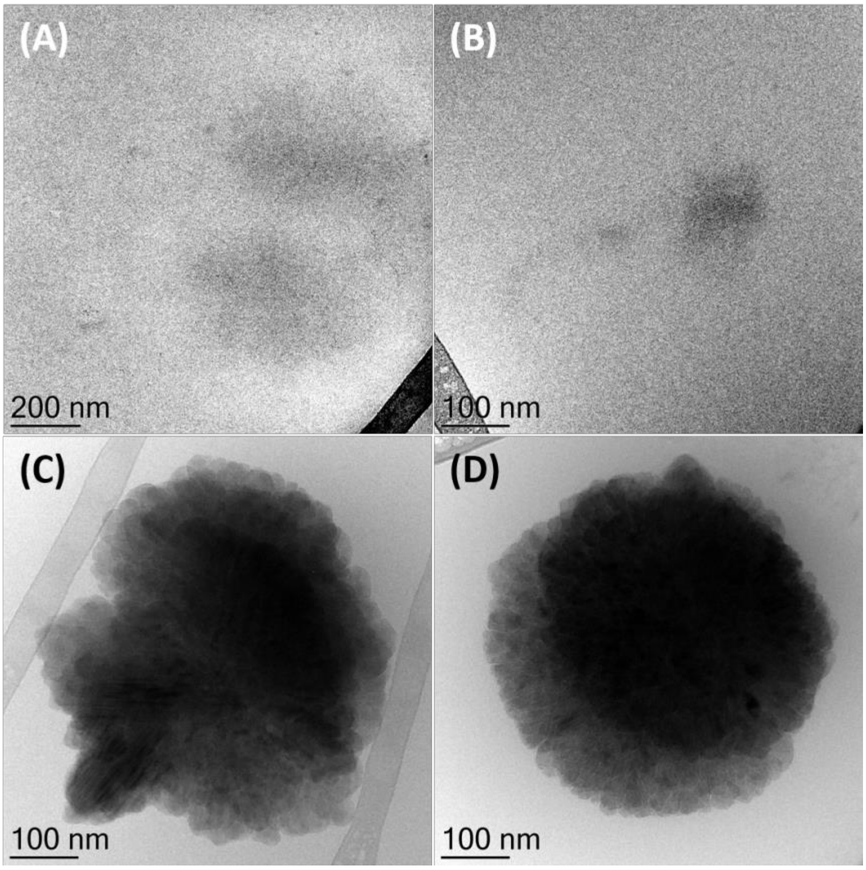

Figure S25. Representative cryo-TEM micrographs of mineral structures observed during the post-nucleation stages at (A, C) pH 8.5 and (B, D) pH 8.0.

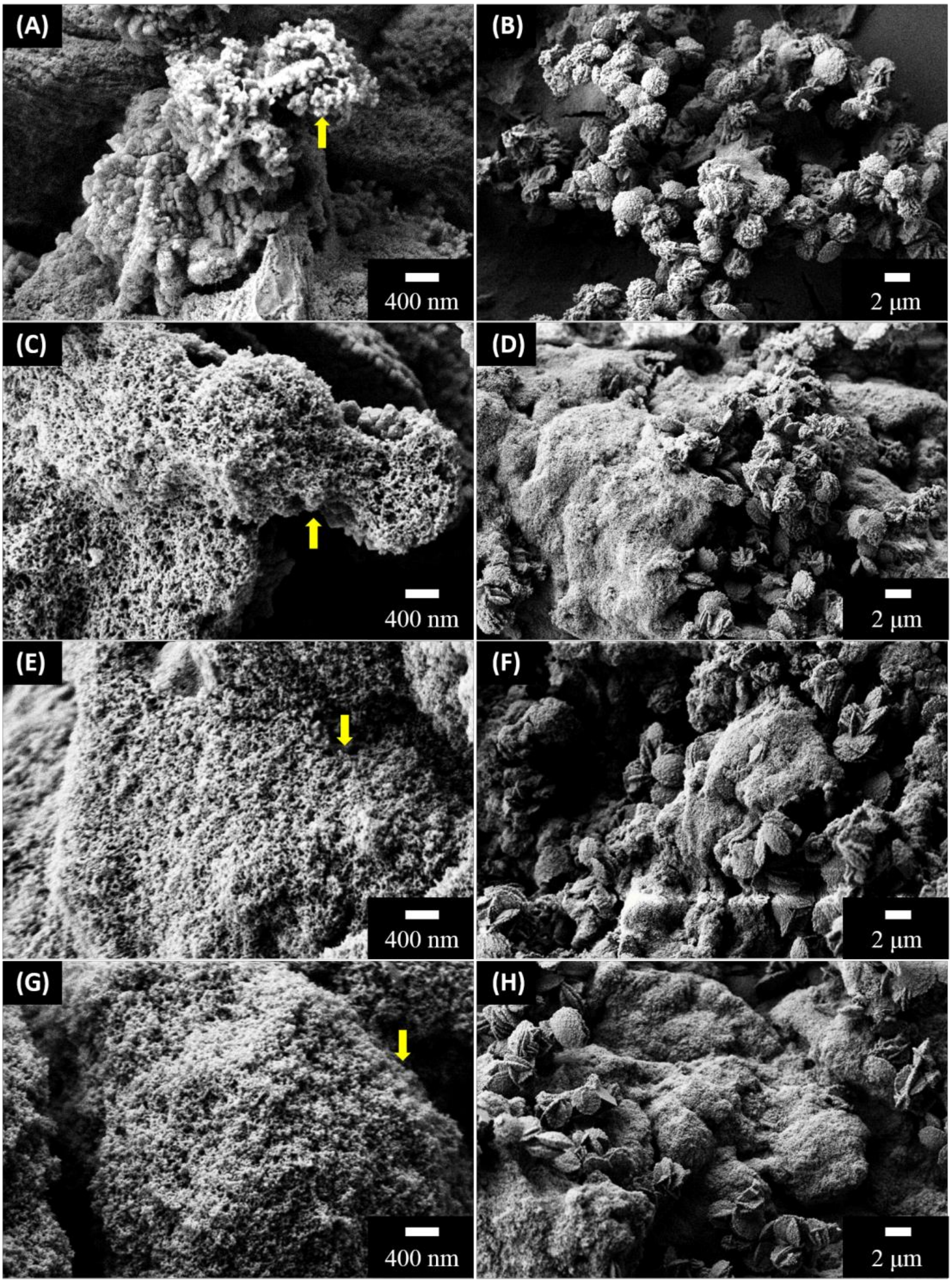

Figure S26. Representative SEM images of mineral particles formed after nucleation at (A, B) pH 9.0, (C, D) pH 8.5, (E, F) pH 8.2, and (G, H) pH 8.0. The arrows indicate the nanoparticles constituting ACC (left) and the microparticles represent crystalline calcium carbonate, vaterite (right).

Tables

Table S1. Fractions of carbonate buffer species in the range of pH 7.5 to 9.0. The pK values for calculating the fractions of carbonate species are 6.35 and 10.33[42], respectively.

pH	$\lambda(H_2CO_3)$	$\lambda(HCO_3^-)$	$\lambda(CO_3^{2-})$
9.0	0.0021	0.9533	0.0446
8.8	0.0034	0.9680	0.0286
8.5	0.0069	0.9786	0.0145
8.2	0.0138	0.9789	0.0073
8.0	0.0218	0.9736	0.0046
7.5	0.0660	0.9326	0.0014

Table S2. Equilibrium constants for the formation of calcium bicarbonate ($CaHCO_3^+$) and calcium carbonate ($CaCO_3^0$) ion pairs, as well as the ratio of bound HCO_3^- and bound CO_3^{2-} ions in ion associates at different pH values. Note that the ion pairing is considered as a simplified model of ion association and yields an average equilibrium constant of pre-nucleation cluster formation in the case of calcium carbonate. The errors represent ± 1-σ-standard deviation for N = 3 repetitions.

pH	$\log K_{CaHCO_3^+}$	$\log K_{CaCO_3^0}$	$\frac{c(CaHCO_3^+)}{c(CaCO_3^0)}$
8.5	1.39 ± 0.11	3.22 ± 0.10	0.98 ± 0.22
8.2	1.26 ± 0.04	3.23 ± 0.03	1.44 ± 0.10
8.0	1.34 ± 0.04	3.24 ± 0.03	2.72 ± 0.18

Table S3. Microscopic binding parameters (x_1 and K_1) and macroscopic equilibrium constant of calcium carbonate ion association (K'_1 and $K_{CaCO_3^0}$) at given pH conditions. The standard deviation of $K_{CaCO_3^0}$ represents data points of the linear pre-nucleation regime collected at time intervals of 10 s.

pH	x_1[a]	K_1[a]	K'_1[a]	$K_{CaCO_3^0}$
8.5	1.0740 ± 0.0003	1547 ± 8	1662 ± 9	1716 ± 377
8.2	1.0760 ± 0.0006	1538 ± 14	1655 ± 15	1717 ± 138
8.0	1.0963 ± 0.0005	1497 ± 13	1641 ± 15	1740 ± 131

[a] Error assessments do not consider the errors from CO_2 out-diffusion, which are difficult to quantify. Thus, the uncertainties of binding parameters should be somewhat larger than the derived errors.

Table S4. Derived binding parameters (x_2 and K_2) in a microscopic perspective and macroscopic equilibrium constant of calcium bicarbonate ion association (K'_2 and $K_{CaHCO_3^+}$). The standard deviations of $K_{CaHCO_3^+}$ were evaluated from data points in the pre-nucleation stage recorded at time intervals of 10 s.

pH	**x_2** [a]	**K_2** [a]	**K'_2** [a]	**$K_{CaHCO_3^+}$**
8.5	-0.2521 ± 0.0021	-95.8 ± 1.3	24.2 ± 0.1	25.0 ± 6.0
8.2	-0.1791 ± 0.0016	-98.7 ± 2.0	17.7 ± 0.2	18.4 ± 1.7
8.0	-0.1690 ± 0.0007	-124.3 ± 1.7	21.0 ± 0.2	22.1 ± 1.8

[a] Errors of binding parameters should be somewhat larger than the derived errors because the errors due to CO_2 out-diffusion are not included in the calculated errors since they are difficult to assess.

Table S5. Enthalpy, entropy and standard ion pairing free energy for Ca-HCO_3^+ as determined from the titration experiments and AMOEBA simulations in this work, as well as from previous experiments.

	ΔH (kJ/mol)	**ΔS (J/mol K)**	**ΔG(300K) (kJ/mol)**
This work (exp)	–	–	-7.6
AMOEBA	10.3 ± 2	61 ± 7	-7.8
Plummer & Busenberg[36]	7.3 ± 2	46 ± 6	-6.3
Martynova *et al.*[43]	20.4 ± 1	93 ± 3	-7.3
Jacobson & Langmuir[44]	24.6 ± 2	102 ± 5	-5.8

Table S6. Formation free energies for various calcium-carbonate-bicarbonate clusters computed using well-tempered metadynamics simulations and the AMOEBA polarizable force field developed in this work. $\Delta\Delta G_H$ indicates the change in the bicarbonate deprotonation free energy relative to the isolated anion, and ΔpK_a is the corresponding downward shift in the proton acidity. See Figure S12 for a description of the thermodynamic cycle used to compute the shift in the carbonate proton acidity.

	ΔG (kJ/mol)	**$\Delta\Delta G_H$ (J/mol K)**	**ΔpK_a**
Ca-HCO_3	-7.8	-9.5	1.66
Ca-CO_3	-17.3		
CaHCO_3-Ca	+2.4	-17.3-9.2-(-7.8+2.4) = -21.1	3.68
CaCO_3-Ca	-9.2		
CaHCO_3-HCO_3	-2.9	-6.6	1.15
CaHCO_3-CO_3	-9.5		
CaCO_3-HCO_3	-0.4	-5.2	0.91
CaCO_3-CO_3	-5.6		
Ca$[HCO_3]_2$-HCO_3	+3.3	-6.5	1.13
Ca$[HCO_3]_2$-CO_3	-3.2		

Table S7. Proton acidity estimated from the cluster formation free energies computed in this work and simple thermodynamic cycles similar to the one shown in Figure S12.

	pK_a
HCO_3^-	10.3 (experimental)
$CaHCO_3^+$	8.6
$CaHCO_3Ca^{3+}$	6.6
$Ca[HCO_3]_2^0$	9.1
$CaCO_3HCO_3^-$	9.4
$Ca[HCO_3]_3^-$	9.1

Table S8. Comparison of calculated vs. experimental lattice parameters (lengths in Å, angles in degrees) for bulk crystalline phases.

Mineral	**Lattice parameter**	**Experiment**	**Calculated**	**Error (%)**
Calcite[45]	a	4.988	5.0173	+0.6
($CaCO_3$)	c	17.061	16.8671	-1.1
Nahcolite[46]	a	7.51	7.3532	-2.1
($NaHCO_3$)	b	9.70	9.7634	+0.7
	c	3.53	3.5028	-0.8
	β	93.32	95.78	+2.6
Trona[47]	a	20.36	20.2759	-0.4
($Na_3(CO_3)(HCO_3)(H_2O)_2$)	b	3.48	3.4593	-0.6
	c	10.29	10.3345	+0.4
	β	106.48	108.05	+1.5
Wegscheiderite[48]	a	3.4762	3.4709	-0.2
($Na_5(CO_3)(HCO_3)_3$)	b	10.0393	10.1095	+0.7
	c	15.5969	15.5307	-0.4
	α	107.77	108.37	+0.6
	β	95.59	95.49	-0.1
	γ	95.03	95.27	+0.3
Monohydrocalcite[49]	a	10.5547	10.5259	-0.3
($CaCO_3 \cdot H_2O$)	c	7.5644	7.5717	+0.1
Ikaite[50]	a	8.792	8.6716	-1.4
($CaCO_3 \cdot 6H_2O$)	b	8.310	8.2667	-0.5
	c	11.021	10.8457	-1.6
	β	110.53	109.17	-1.2

Table S9. Comparison of calculated vs. experimental isotropic chemical shifts (in ppm) for bulk crystalline phases, with line widths in parenthesis for experimental values. Experimental data are taken from Nebel *et al.*[40], *Inorg. Chem.*, **47**, 7874 (2008), except for trona, which comes from Feng *et al.*[51], *Am. Miner.*, **91**, 957 (2006). A dash signifies an absence of available experimental data, while N/A indicates that this chemical shift is not applicable to this mineral. For calculated values, parenthesis gives the species and average value, where appropriate.

Mineral	**^{13}C (expt)**	**^{13}C (calc)**	**^{1}H (expt)**	**^{1}H (calc)**
Calcite	168.21 (0.25)	167.53	N/A	N/A
Nahcolite	164.47 (2.2)	164.47	14.16 (1.2)	14.16
Trona	-	166.78, 167.71	18.6	19.36 (HCO_3) 3.88–7.39 (H_2O, 5.60)
Wegscheiderite	-	162.44, 162.74 (isolated HCO_3)	-	13.92, 14.82 (isolated HCO_3) 19.53, 19.62 (bridging HCO_3)
Monohydrocalcite	171.10 (2.1)	171.45, 171.71, 171.89	5.43 (1.6)	4.28–6.25 (H_2O, 5.10)
Ikaite	167.98 (0.9)	168.02	-	4.85–6.55 (H_2O, 5.55)

Table S10. Calculated isotropic chemical shifts (in ppm) for a number of theoretically constructed models of amorphous calcium carbonate (ACC), with and without bicarbonate defects. Here “wet” ACC refers to a model that has one mole of water per formula unit, while “dry” ACC has the composition $CaCO_3$. Where there are multiple species of the same type, both the range of values and average (av) are given. For cases where more than one configuration was considered, the internal energy relative to the most stable minimum is given.

System	Model Number	^{13}C (calc)	^{1}H (calc)	ΔU (kJ/mol)
Dry ACC	-	162.89–171.89, av = 167.20 (CO_3)	N/A	-
Wet ACC	-	163.87–171.27, av = 167.94 (CO_3)	0.54–12.90, av = 5.42 (H_2O)	-
Dry ACC HCO_3^- substitution	1	153.08 (HCO_3)	10.50 (HCO_3)	15.5
	2	153.80 (HCO_3)	6.92 (HCO_3)	9.3
	3	163.17 (HCO_3)	10.99 (HCO_3)	84.4
	4	160.15 (HCO_3)	11.29 (HCO_3)	0.0
Wet ACC HCO_3^- substitution	1	162.69 (HCO_3)	13.03 (HCO_3)	10.3
	2	162.40 (HCO_3)	12.11 (HCO_3)	0.0
	3	153.01 (HCO_3)	7.35 (HCO_3)	48.0
	4	159.15 (HCO_3)	9.85 (HCO_3)	20.6
Wet ACC 2xHCO_3^- substitution, with Ca^{2+} vacancy	1	160.82,163.87 (HCO_3)	12.82, 13.30 (HCO_3)	0.0
	2	156.81,159.80 (HCO_3)	10.73,12.08 (HCO_3)	41.8

Table S11. Stoichiometry and thermal stabilities of ACC samples at pH 8.0 and 7.5 acquired from TGA and DSC profiles based on two independent repetitions.

pH	Stoichiometry	Thermal Stability (°C)	Enthalpy of ACC crystallization (ΔH_{cryst} kJ/mol)
8.0	$Ca(CO_3)_{0.95}(HCO_3)_{0.05}(H_2O)_{0.87}$	359 ± 0	-42.51 ± 11.90
7.5	$Ca(CO_3)_{0.97}(HCO_3)_{0.03}(H_2O)_{0.87}$	350 ± 0	-44.22 ± 20.06

AMOEBA force field parameters in TINKER format

```
      ##############################
      ##                          ##
      ##  Force Field Definition  ##
      ##                          ##
      ##############################


forcefield              AMOEBA-WATER-2003

bond-cubic              -2.55
bond-quartic            3.793125
angle-cubic             -0.014
angle-quartic           0.000056
angle-pentic            -0.0000007
angle-sextic            0.000000022
opbendtype              ALLINGER
opbend-cubic            -0.014
opbend-quartic          0.000056
opbend-pentic           -0.0000007
opbend-sextic           0.000000022
torsionunit             0.5
vdwtype                 BUFFERED-14-7
radiusrule              CUBIC-MEAN
radiustype              R-MIN
radiussize              DIAMETER
epsilonrule             HHG
dielectric              1.0
polarization            MUTUAL
vdw-12-scale            0.0
vdw-13-scale            0.0
vdw-14-scale            1.0
vdw-15-scale            1.0
mpole-12-scale          0.0
mpole-13-scale          0.0
mpole-14-scale          0.4
mpole-15-scale          0.8
polar-12-scale          0.0
polar-13-scale          0.0
polar-14-scale          1.0
polar-15-scale          1.0
polar-14-intra          0.5
direct-11-scale         0.0
direct-12-scale         1.0
direct-13-scale         1.0
direct-14-scale         1.0
mutual-11-scale         1.0
mutual-12-scale         1.0
mutual-13-scale         1.0
mutual-14-scale         1.0

############################################################################################
# atom     1     1    O     "Water_O"
# atom     2     2    H     "Water_H"
# atom     3     3    Ca    "Calcium_Ion_Ca+2"
#--------------------------------------------------
# atom    11    11    C     "Carbonate_C"
# atom    12    12    O     "Carbonate_O"
#--------------------------------------------------
# atom    13    13    C     "Bicarbonate_C"
# atom    14    14    O     "Bicarbonate_O(H)"
# atom    15    15    O     "Bicarbonate_O"
# atom    16    16    H     "Bicarbonate_H"
############################################################################################

#
# The water potential is the modified AMOEBA '03
# M. L. Laury, L.-P. Wang, V. S. Pande, T. Head-Gordon, and J. W. Ponder,
# Revised Parameters for the AMOEBA Polarizable Atomic Multipole Water Model
# J. Phys. Chem. B, vol. 119, no. 29, pp. 9423-9437, Jul. 2015.
#

atom          1    1    O     "Water_O"                      8    15.999    2
atom          2    2    H     "Water_H"                      1     1.008    1

vdw           1               3.4050     0.1100
vdw           2               2.6550     0.0135      0.910
```

```
bond          1    2          556.85     0.9572

angle         2    1    2      48.70     108.50

ureybrad      2    1    2      -7.60     1.5326

multipole     1   -2   -2              -0.51966
                                        0.00000    0.00000    0.14279
                                        0.37928
                                        0.00000   -0.41809
                                        0.00000    0.00000    0.03881
multipole     2    1    2               0.25983
                                       -0.03859    0.00000   -0.05818
                                       -0.03673
                                        0.00000   -0.10739
                                       -0.00203    0.00000    0.14412

polarize      1          0.8370     0.3900      2
polarize      2          0.4960     0.3900      1

####################

atom          3    3    Ca    "Calcium_Ion_Ca+2"            20    40.078    0

vdw           3               3.5500     0.3500

multipole     3    0    0               2.00000
                                        0.00000    0.00000    0.00000
                                        0.00000
                                        0.00000    0.00000
                                        0.00000    0.00000    0.00000

polarize      3          0.5500     0.1585

####################

atom         11   11    C     "Carbonate_C"                  6    12.011    3
atom         12   12    O     "Carbonate_O"                  8    15.995    1

vdw          11               3.6500     0.1060
vdw          12               3.5950     0.1050

bond         11   12          505.00     1.3100

angle        12   11   12     120.0      120.00

strbnd       12   11   12     11.50      11.50

opbend       12   11   12   12           242.00

multipole    11   12   12               1.31911
                                        0.00000    0.00000    0.00000
                                        0.02323
                                        0.00000   -0.04646
                                        0.00000    0.00000    0.02323
multipole    12   11   12              -1.10637
                                        0.00000    0.00000    0.13933
                                       -0.47678
                                        0.00000   -0.28195
                                        0.00000    0.00000    0.75873

polarize     11          1.3340     0.3900     12
polarize     12          0.8370     0.3900     11

####################

atom         13    13    C      "Bicarbonate_C"            6     12.011    3
atom         14    14    O      "Bicarbonate_OH"           8     15.995    2
atom         15    15    O      "Bicarbonate_O"            8     15.995    1
atom         16    16    H      "Bicarbonate_H"            8      1.008    1

vdw          13               3.670     0.1060
vdw          14               3.680     0.0950
vdw          15               3.680     0.0950
vdw          16               2.255     0.0150     0.91


bond         13   15          605.00    1.2525
```

```
bond         13   14          331.60    1.4540
bond         14   16          514.40    0.9737

angle        13   14   16      49.60    108.70
angle        14   13   15      92.30    113.48
angle        15   13   15     102.5     133.04


strbnd       14   13   15     18.70      18.70
strbnd       15   13   15     18.70      18.70

opbend       14   13   15   15           145.0
opbend       15   13   14   15           145.0


torsion      15   13   14   16      0.000 0.0 1   4.950 180.0 2   0.000 0.0 3


multipole     13  -15  -15               1.24761
                                        -0.02780    0.00000   -0.12783
                                         0.04256
                                         0.00000   -0.18474
                                         0.06473    0.00000    0.14218
multipole     14   13   16              -0.62219
                                         0.23755    0.00000   -0.04595
                                         0.61449
                                         0.00000   -0.46373
                                        -0.29267    0.00000   -0.15076
multipole     15   13   14              -0.92733
                                        -0.04328    0.00000   -0.05066
                                        -0.30699
                                         0.00000    0.01888
                                        -0.03525    0.00000    0.28811
multipole     16   14   13               0.22924
                                         0.00476    0.00000   -0.08657
                                         0.00000
                                         0.00000    0.00000
                                         0.00000    0.00000    0.00000

polarize     13               1.334      0.390      14   15
polarize     14               0.837      0.390      13   16
polarize     15               0.837      0.390      13
polarize     16               0.496      0.390      14
```

References

[1] A. E. Bennett, C. M. Rienstra, M. Auger, K. V. Lakshmi, R. G. Griffin, *J. Chem. Phys.* **1995**, *103*, 6951–6958.

[2] A. Bielecki, A. C. Kolbert, H. J. M. De groot, R. G. Griffin, M. H. Levitt, in *Adv. Magn. Opt. Reson.* (Ed.: W.S. Warren), Academic Press, **1990**, pp. 111–124.

[3] R. Demichelis, P. Raiteri, J. D. Gale, D. Quigley, D. Gebauer, *Nat. Commun.* **2011**, *2*, 590.

[4] J. W. Ponder, C. Wu, P. Ren, V. S. Pande, J. D. Chodera, M. J. Schnieders, I. Haque, D. L. Mobley, D. S. Lambrecht, R. A. DiStasio, M. Head-Gordon, G. N. I. Clark, M. E. Johnson, T. Head-Gordon, *J. Phys. Chem. B* **2010**, *114*, 2549–2564.

[5] P. Raiteri, A. Schuitemaker, J. D. Gale, *J. Phys. Chem. B* **2020**, *124*, 3568–3582.

[6] F. Weigend, R. Ahlrichs, *Phys. Chem. Chem. Phys.* **2005**, *7*, 3297–3305.

[7] J.-D. Chai, M. Head-Gordon, *J. Chem. Phys.* **2008**, *128*, 084106.

[8] S. Grimme, J. Antony, S. Ehrlich, H. Krieg, *J. Chem. Phys.* **2010**, *132*, 154104.

[9] L. Lagardère, L.-H. Jolly, F. Lipparini, F. Aviat, B. Stamm, Z. F. Jing, M. Harger, H. Torabifard, G. Andrés Cisneros, M. J. Schnieders, N. Gresh, Y. Maday, P. Y. Ren, J. W. Ponder, J.-P. Piquemal, *Chem. Sci.* **2018**, *9*, 956–972.

[10] The PLUMED consortium, *Nat. Methods* **2019**, *16*, 670–673.

[11] G. A. Tribello, M. Bonomi, D. Branduardi, C. Camilloni, G. Bussi, *Comput. Phys. Commun.* **2014**, *185*, 604–613.

[12] A. Laio, M. Parrinello, *Proc. Natl. Acad. Sci.* **2002**, *99*, 12562–12566.

[13] P. Raiteri, A. Laio, F. L. Gervasio, C. Micheletti, M. Parrinello, *J. Phys. Chem. B* **2006**, *110*, 3533–3539.

[14] A. Barducci, G. Bussi, M. Parrinello, *Phys. Rev. Lett.* **2008**, *100*, 020603.

[15] P. Raiteri, R. Demichelis, J. D. Gale, *J. Phys. Chem. C* **2015**, *119*, 24447–24458.

[16] N. A. Garcia, R. I. Malini, C. L. Freeman, R. Demichelis, P. Raiteri, N. A. J. M. Sommerdijk, J. H. Harding, J. D. Gale, *Cryst. Growth Des.* **2019**, *19*, 6422–6430.

[17] M. L. Laury, L.-P. Wang, V. S. Pande, T. Head-Gordon, J. W. Ponder, *J. Phys. Chem. B* **2015**, *119*, 9423–9437.

[18] F. Neese, *Wiley Interdiscip. Rev. Comput. Mol. Sci.* **2018**, *8*, e1327.

[19] F. Neese, F. Wennmohs, A. Hansen, U. Becker, *Chem. Phys.* **2009**, *356*, 98–109.

[20] V. Barone, M. Cossi, *J. Phys. Chem. A* **1998**, *102*, 1995–2001.

[21] A. L. Goodwin, F. M. Michel, B. L. Phillips, D. A. Keen, M. T. Dove, R. J. Reeder, *Chem. Mater.* **2010**, *22*, 3197–3205.

[22] J. W. Singer, A. Ö. Yazaydin, R. J. Kirkpatrick, G. M. Bowers, *Chem. Mater.* **2012**, *24*, 1828–1836.

[23] P. Raiteri, J. D. Gale, *J. Am. Chem. Soc.* **2010**, *132*, 17623–17634.

[24] S. J. Clark, M. D. Segall, C. J. Pickard, P. J. Hasnip, M. I. J. Probert, K. Refson, M. C. Payne, *Z. Für Krist. - Cryst. Mater.* **2009**, *220*, 567–570.

[25] G. Stefan, *J. Comput. Chem.* **2006**, *27*, 1787–1799.

[26] E. R. McNellis, J. Meyer, K. Reuter, *Phys. Rev. B* **2009**, *80*, 205414.

[27] J. R. Yates, C. J. Pickard, F. Mauri, *Phys. Rev. B* **2007**, *76*, 024401.

[28] C. J. Pickard, F. Mauri, *Phys. Rev. B* **2001**, *63*, 245101.

[29] D. Gebauer, A. Völkel, H. Cölfen, *Science* **2008**, *322*, 1819–1822.

[30] M. Kellermeier, P. Raiteri, J. K. Berg, A. Kempter, J. D. Gale, D. Gebauer, *ChemPhysChem* **2016**, *17*, 3535–3541.

[31] G. Scatchard, *Ann. N. Y. Acad. Sci.* **1949**, *51*, 660–672.

[32] M. Kellermeier, A. Picker, A. Kempter, H. Cölfen, D. Gebauer, *Adv. Mater.* **2014**, *26*, 752–757.

[33] M. Farhadi-Khouzani, D. M. Chevrier, P. Zhang, N. Hedin, D. Gebauer, *Angew. Chem. Int. Ed.* **2016**, *55*, 8117–8120.

[34] I. Greenwald, *J. Biol. Chem.* **1941**, *141*, 789–796.

[35] E. W. Moore, H. J. Verine, *Am. J. Physiol.* **1981**, *241*, G182-190.

[36] L. N. Plummer, E. Busenberg, *Geochim. Cosmochim. Acta* **1982**, *46*, 1011–1040.

[37] J.-Y. Gal, J.-C. Bollinger, H. Tolosa, N. Gache, *Talanta* **1996**, *43*, 1497–1509.

[38] A. De Visscher, J. Vanderdeelen, E. Königsberger, B. R. Churagulov, M. Ichikuni, M. Tsurumi, *J. Phys. Chem. Ref. Data* **2012**, *41*, 013105-013105–67.

[39] M. P. Andersson, J. D. Rodriguez-Blanco, S. L. S. Stipp, *Geochim. Cosmochim. Acta* **2016**, *176*, 198–205.

[40] H. Nebel, M. Neumann, C. Mayer, M. Epple, *Inorg. Chem.* **2008**, *47*, 7874–7879.

[41] J. P. Yesinowski, H. Eckert, *J. Am. Chem. Soc.* **1987**, *109*, 6274–6282.

[42] D. R. Lide, *Handbook of Chemistry and Physics*, CRC Press, Boca Raton, **1994**.

[43] O. I. Martynova, L. G. Vasina, S. A. Pozdniakova, *Desalination* **1974**, *15*, 259–265.

[44] R. L. Jacobson, D. Langmuir, *Geochim. Cosmochim. Acta* **1974**, *38*, 301–318.

[45] S. A. Markgraf, R. J. Reeder, *Am. Mineral.* **1985**, *70*, 590–600.

[46] W. H. Zachariasen, *J. Chem. Phys.* **1933**, *1*, 634–639.

[47] C. S. Choi, A. D. Mighell, *Acta Crystallogr. B* **1982**, *38*, 2874–2876.

[48] N. G. Fernandes, R. Tellgren, I. Olovsson, *Acta Crystallogr. B* **1990**, *46*, 466–474.

[49] I. P. Swainson, *Am. Mineral.* **2008**, *93*, 1014–1018.

[50] *Z. Für Krist. - Cryst. Mater.* **2010**, *163*, 227–231.

[51] J. Feng, Y. J. Lee, R. J. Reeder, B. L. Phillips, *Am. Mineral.* **2006**, *91*, 957–960.

Author Contributions

Yu-Chieh Huang performed titration experiments, sample preparations, NMR data evaluation, measurements of IR, SEM and EDX, as well as corresponding data analyses, figure design and writing of a first manuscript draft. Ashit Rao contributed to the first draft and the manuscript writing with valuable ideas and discussions. Shing-Jong Huang conducted NMR measurements and data evaluation. Chun-Yu Chang conducted NMR sample packing and assisted in NMR measurements. Markus Drechsler conducted cryo-TEM measurements and analyses. Jennifer Knaus performed TGA and DSC measurements and participated in valuable discussions of the results. Jerry C. C. Chan supervised the NMR work, contributed to NMR data evaluation, the writing of the initial draft and also provided valuable ideas and discussions. Paolo Raiteri and Julian D. Gale performed the quantum mechanical calculations and molecular dynamics simulations, corresponding evaluations, designed the corresponding display items, wrote the corresponding sections of the manuscript and provided valuable ideas and discussions. Denis Gebauer developed the project idea, and supervised the experimental work and the writing of the original draft.